Melting of hybrid organic–inorganic perovskites

Bikash Kumar Shaw, Ashlea R Hughes, Maxime Ducamp, Stephen Moss, Anup Debnath, Adam F Sapnik, Michael F Thorne, Lauren N Mchugh, Andrea Pugliese, Dean S Keeble, et al.

Melting of Hybrid Organic-Inorganic Perovskites

Bikash Kumar Shaw[1], Ashlea R. Hughes[2], Maxime Ducamp[3], Stephen Moss[2], Anup Debnath[4], Adam F. Sapnik[1], Michael F. Thorne[1], Lauren N. McHugh[1], Andrea Pugliese[2], Dean S. Keeble[5], Philip Chater[5], Juan M. Bermudez-Garcia[1,6], Xavier Moya[1], Shyamal K. Saha[4], David A. Keen[7], François-Xavier Coudert[3], Frédéric Blanc[2,8] and Thomas D. Bennett*[1]

[1] Department of Materials Science and Metallurgy, University of Cambridge, CB3 0FS, UK.

[2] Department of Chemistry, University of Liverpool, Crown Street, Liverpool L69 7ZD, UK.

[3] Chimie ParisTech, PSL University, CNRS, Institut de Recherche de Chimie Paris, 75005 Paris, France.

[4] School of Materials Sciences, Indian Association for the Cultivation of Science, Jadavpur, Kolkata 700032, India.

[5] Diamond Light Source Ltd, Diamond House, Harwell Campus, Didcot, Oxfordshire, OX11 0DE, UK.

[6] University of A Coruna, QuiMolMat Group, Dpt. Chemistry, Faculty of Science and Advanced Scientific Research Center (CICA), Zapateira, 15071 A Coruña, Spain.

[7] ISIS Facility, Rutherford Appleton Laboratory, Harwell Campus, Didcot, Oxon OX11 0QX, UK.

[8] Stephenson Institute for Renewable Energy, University of Liverpool, Crown Street, Liverpool L69 7ZD, UK.

Email: tdb35@cam.ac.uk

Abstract

Several hybrid materials from the metal-organic framework (MOF) family have been demonstrated to form stable liquids at high temperature. Quenching then results in the formation of melt-quenched MOF-glasses, which retain the three-dimensional inorganic-organic bonding of the crystalline phase. The properties of this new class of hybrid glass are of intense interest in both coordination polymer and glass domains. The phenomenon is however still limited to several structures.

Hybrid perovskites occupy a prominent position within solid-state materials chemistry due to their functional properties such as ion transport, photoconductivity, ferroelectricity and multiferroicity. Here we show that a series of dicyanamide-based hybrid organic-inorganic perovskites undergo melting. Our combined experimental-computational approach demonstrates that they form glasses upon quenching, which largely retain inorganic-organic connectivity. Their very low thermal conductivities (~ 0.2 W m^{-1} K^{-1}), combined with moderate electrical conductivities (10^{-3} – 10^{-5} S m^{-1}) and polymer-like thermo-mechanical properties identify them as a new family of functional glass-formers.

Introduction

ABX_3 hybrid organic-inorganic perovskites (HOIPs) are an emerging family of materials, where *A* = organic cation, *B* = metal ion and *X* = bridging ligand. The family occupies a prominent position within solid state chemistry and materials science due to interest in their utility in e.g. ionic transport, ferroelectric, luminescent and multiferroic applications.[1-3]

Hybrid lead halide perovskites in particular have been extensively studied for their performance and efficiency in photovoltaic devices.[4,5] The replacement of the halide ion by flexible bidentate bridging ligands, such as formate [$HCOO^-$],[6] hypophosphite [H_2POO^-][7] and dicyanamide [dca, $N(CN)_2^-$][8] gives rise to an even wider array of functional properties, while preserving their three-dimensional coordination polymer structures.[9]

Crystalline materials dominate the field of HOIP research, and show rich structural behaviour such as octahedral tilting, columnar shifts and molecular disordering associated with phase transitions.[10] Non-crystalline materials receive comparatively little attention, though the reversible pressure-induced amorphization of three dimensional methylammonium lead halide perovskites has been studied,[11,12] alongside melting of the two-dimensional layered HOIP series [$(C_4H_9NH_3)_2MI_4$] (M = Ge, Sn, Pb).[13]

Solid-liquid transitions have however started to be reported in the related family of three-dimensional metal-organic frameworks (MOFs). For example, the melt-quenching of several $Zn(C_3H_3N_2)_2$ structures results in the formation of a new category of glasses, which are structurally similar to silica glass, yet contain linked inorganic and organic components.[14] Routes to expand hybrid glasses are highly sought after, though the limited chemical variance within both glass-forming MOFs and lower dimensionality coordination polymers mean only a relatively small number have been reported.

Motivated by the great chemical variability across the dense ABX_3 perovskite family, in this report we extend the phenomena of melting and melt-quenching in HOIPs. Three [TPrA][$M(dca)_3$] (TPrA = tetrapropylammonium, $(CH_3CH_2CH_2)_4N^+$, M = Mn^{2+},

Fe^{2+}, Co^{2+}) materials were selected for study due to the multiple possible coordination modes possible for the dca ligands, which bridge transition metal cations through the N atom in $\mu_{1,5}$ end-to-end connectivity (**Fig. 1a**). At room temperature, both [TPrA][Co(dca)$_3$] and [TPrA][Fe(dca)$_3$] crystallise in the orthorhombic space group (*Pnna*), as opposed to the tetragonal Mn analogue, which crystallizes in $P\bar{4}2_1c$.[15]

In this work, we show that these materials melt at temperatures lower than existing MOFs, comply with the Lindemann criteria for melting, and investigate de-coordination and decomposition processes in the family. Recrystallisation observed in lower dimensional zinc phosphate coordination polymer glasses may be avoided,[16] whilst the presence of organic cations distinguishes them from the three-dimensional MOFs found to melt thus far. We also show that the glassy products demonstrate potentially useful thermal and electrical conductivities.

Results

Glass Formation and Thermal Properties

Single crystals of [TPrA][M(dca)$_3$] (M = Mn, Fe, Co) were obtained by solvent layering, following previously reported procedures (**Methods**, **Supplementary Fig. 1**).[8,15] Thermogravimetric analysis revealed decomposition temperatures (T_d) of 281 ºC, 273 ºC and 267 ºC for the Mn, Fe and Co analogues respectively (**Supplementary Fig. 2**), in agreement with prior literature.[17] Differential scanning calorimetry (DSC) was carried out on each sample, and identified sharp endotherms at temperatures far in excess of the reported solid-solid polymorphic phase transitions.[8,15] These correspond to unreported melting (T_m) at 271 ºC, 263 ºC and 230 ºC for the Mn, Fe and Co analogues (**Fig. 1b**). Weight losses at T_m were less than 0.5% in all cases. The increase in T_m from Co to Mn follows the trend in the ionic radii $r_{Co} < r_{Fe} < r_{Mn}$, consistent with hard-soft/acid-base theory.

Crystalline samples of [TPrA][M(dca)$_3$] (M = Mn, Fe, Co) were heated in a simultaneous DSC-TGA experiment to temperatures above T_m, before cooling back to room temperature (**see methods**). Liquid-like behaviour was evident from the physical appearance of samples upon cooling from 277 ºC (Mn), 269 ºC (Fe) and 264 ºC (Co), and their amorphous X-ray diffraction patterns (**Supplementary Figs.**

3-6). Partial recrystallisation of a_g[TPrA][Mn(dca)$_3$] and a_g[TPrA][Fe(dca)$_3$] occurred at cooling from lower temperatures. The glasses, in keeping with existing nomenclature on hybrid glasses, are termed a_g[TPrA][M(dca)$_3$] (a_g: melt quenched glass). Subsequent DSC experiments (**see methods**) yielded smooth but very weak changes in the heat flow, indicative of glass transitions (T_g), at temperatures of 223 ºC, 225 ºC and 125 ºC for a_g[TPrA][Mn(dca)$_3$], a_g[TPrA][Fe(dca)$_3$] and a_g[TPrA][Co(dca)$_3$] respectively (**Table 1, Supplementary Fig. 7**). Like ZIF-glasses (T_g/T_m ~ 0.9), a deviation from the empirical "T_g/T_m ~ 2/3" law is observed, (|2/3 - T_g/T_m| = [0.14 - 0.18]).[18] Small weight losses of <0.5% for the Mn, Fe and Co glasses upon heating to their respective T_g's were noted (**Supplementary Fig. 8)**.

Thermomechanical analysis (TMA) was performed on the a_g[TPrA][M(dca)$_3$] samples, and the resultant dilatometric softening temperatures (T_f), i.e. where the solid glass began to transform into a softer state, used to corroborate the values of T_g extracted from DSC measurements (**Fig. 1c**, **Supplementary Fig. 9**). Frequency-dependent dynamic mechanical analysis (DMA), a more sensitive method of obtaining the glass transition temperature, was performed and identified T_g values of 185 ºC, 219 ºC and 145 ºC for a_g[TPrA][Mn(dca)$_3$], a_g[TPrA][Fe(dca)$_3$], and a_g[TPrA][Co(dca)$_3$], using the maximum value of the loss modulus (**Fig. 1d**, **Supplementary Fig. 10**).[16] These agree well with those obtained from TMA and DSC measurements (**Table 1**).

The shift in T_g to higher temperature with increasing applied frequency was used to calculate activation energies (E_a) associated with T_g using the Arrhenius equation (**1**) (**Table 1**, **Supplementary Fig. 11**, **Supplementary Table 1**).

$$\log \frac{f_1}{f_2} = \frac{E_a}{R}\left(\frac{1}{T_{g_2}} - \frac{1}{T_{g_1}}\right) \quad (1)$$

where f_1, f_2 = applied frequencies, T_{g_1}, T_{g_2}= glass transitions at the applied frequencies, R = ideal gas constant.

Delineating Decoordination and Decomposition

^{13}C Nuclear Magnetic Resonance (NMR) spectra of [TPrA][Mn(dca)$_3$], [TPrA][Fe(dca)$_3$] and [TPrA][Co(dca)$_3$] before and after melt-quenching were

obtained (**Fig. 2**, **Supplementary Figs. 12-14**).[19-21] Spectra of [TPrA][Fe(dca)$_3$] and [TPrA][Co(dca)$_3$] contain one resonance in the 200 to -100 ppm region per type of carbon in the TPrA cation and two (or more) poorly resolved resonances around 3900 ppm for the N*C*N carbon of the dca anions (see below and **Supplementary Figs. 15**, **16** for spectral assignment). In contrast, in crystalline [TPrA][Mn(dca)$_3$] where the NMR lines are much narrower, resonances for each type of carbons in the TPrA and dca ions (e.g. the N*C*N resonance appears as two resolved shifts of 7 and 3 ppm in a 2:1 ratio) can be observed (**Supplementary Fig. 17**). These observations are consistent with the phases expected based on previous reports of phase transitions in the family (**see methods**).[15] The spectra were assigned based on known chemical shift values for TPrA in diamagnetic systems,[22] spatial proximity to the metal centres and ^{13}C-edited experiment using ^{1}H ^{13}C TEDOR[21,23] (transferred echo double resonance) experiments that filter out any non-protonated carbons (**Supplementary Figs. 12-14**). The absence of ^{13}C signal at *ca*. 3900 ppm in both [TPrA][Fe(dca)$_3$] and [TPrA][Co(dca)$_3$] TEDOR spectra strongly supports its assignment to the N*C*N carbon of the dca anions, which contains the only quaternary carbon amongst both TPrA and dca ions. It is therefore postulated that the very large paramagnetic shifts observed in dca result from its $\mu_{1,5}$ bonding mode to two metal centres (**Fig. 1a**). Notably, the N*C*N carbon within the [TPrA][Fe(dca)$_3$] and [TPrA][Co(dca)$_3$] materials appears at a very similar chemical shift, which is also seen elsewhere in literature.[24] The ^{13}C shifts of the TPrA cation are significantly less affected due to the greater distance of this species from the metal centres (**Fig. 1a**), whilst the different chemical shift of the dca ligand in crystalline [TPrA][Mn(dca)$_3$] (*ca*. 5 ppm, **Fig. 2**, **Supplementary Fig. 12 and Supplementary Table 2**) is ascribed to the difference in magnetic susceptibility of Mn^{2+}, in comparison to Fe^{2+} and Co^{2+}. This yields smaller anisotropic bulk magnetic susceptibility broadening in the former, consistent with ^{7}Li MAS NMR of $LiMPO_4$, M = Mn, Fe, Co.[19,24]

Comparison of the spectra of crystalline and glass samples (**Fig. 2**, **Supplementary Figs. 12-14**) shows similar chemical shifts in the TPrA region, suggesting that the 'A' site cation remains intact during the melt-quenching process. No resonances for the dca carbons are observed in their paramagnetic NMR regions for any of the quenched glasses due to a likely decrease in the transverse magnetization decay time constant with refocused inhomogeneous broadening T_2' and increase in line

broadening upon vitrification and hence, an increase in paramagnetic broadening of the glasses.

Experimental evidence for the decoordination of dca ligands during the melting process arises from an additional resonance at 120 ppm in the spectra for a_g[TPrA][Fe(dca)$_3$], which is assigned to a 'free' dca ligand.[25] A further peak at 159 ppm, combined with the appearance of two (weak) absorption bands at 1629-1634 cm^{-1} and 802-806 cm^{-1} in the infra-red spectra for all glasses, also indicates a degree of ligand decomposition upon melting (**Supplementary Fig. 18**).[17,25,26]

Liquid phase ^{1}H and ^{13}C NMR spectra (**Supplementary Figs. 19-24**) and high-resolution mass spectrometry (HRMS) data (**Supplementary Figs. 25-30**) of digested samples were collected. The ^{1}H and ^{13}C spectra for [TPrA][Co(dca)$_3$] each contain the expected three resonances of [TPrA] while NMR signals for an H_2O-protonated dca ligand, that is known to exist as an aminonitrile – carbodiimide tautomer as for all cyanamides (**Supplementary Scheme 1**), are observed and further detected in the HRMS data. Specifically, in the NMR data (**Supplementary Figs. 23-24**), the resulting NH appears at 7.5 ppm in the ^{1}H NMR spectrum whilst we ascribe the 153 and 110 ppm signals in the ^{13}C NMR spectrum to the NH=C=N carbodiimide and C≡N nitrile carbons of the dca ligand, respectively,[27] whilst the HRMS data (**Supplementary Figs. 29-30**) reveals both [TPrA] and dca ligands. The similar corresponding NMR and HRMS for a_g[TPrA][Co(dca)$_3$] indirectly confirm the presence of both dca and TPrA ligands. Similar NMR results were obtained with both Mn and Fe samples (**Supplementary Figs. 19-22** and **25-28**), though hyperfine coupling in the NMR spectra induced poor signal-to-noise ratios and spectral broadening that render detection of some of the dca carbons more challenging.

Further evidence for the partial decoordination of dca ligands is provided by diffuse reflectance UV-Vis spectroscopy measurements (**Supplementary Fig. 31**). Specifically, the spectrum for a_g[TPrA][Co(dca)$_3$] contains only two electronic absorption bands. This is in contrast to the three that would be expected for d^7 tetrahedral Co(II), belonging to the $^4A_2 \rightarrow {}^4T_2$, $^4A_2 \rightarrow {}^4T_1$(F), and $^4A_2 \rightarrow {}^4T_1$(P),[28] and consistent with the blue colour (**Supplementary Fig. 32**).[29]

Temperature dependent DC magnetic susceptibility measurements were carried out, and the variation of $\chi_M T$ (χ_M: molar magnetic susceptibility) as a function of T

indicated antiferromagnetic coupling for all samples at low temperatures (**Supplementary Figs. 33, 34**).[30] Room temperature $\chi_M T$ values for the glasses were smaller than those for the crystalline phases, indicating a reduction in oxidation state for a proportion of metal centres. These differences were used to calculate the percentage of metal ions reduced to M(0) upon melt quenching in each case (a_g[TPrA][Mn(dca)$_3$] – 18.7%, a_g[TPrA][Fe(dca)$_3$] – 22.0% and a_g[TPrA][Co(dca)$_3$] – 15.3%), which agree well with those calculated by comparison of XPS spectra (**Supplementary Figs. 35-39**, **Supplementary Table 3**).

Atomistic Insight into Melting

Room temperature total scattering data for [TPrA][M(dca)$_3$] show Bragg peaks arising from long range order (**Supplementary Fig. 40**). In contrast, the data for the corresponding glasses, a_g[TPrA][M(dca)$_3$] reveal smooth broad humps without any major Bragg peaks (**Supplementary Fig. 41**). The X-ray pair distribution functions (PDFs), $D(r)$, were extracted after appropriate data corrections (**Figs. 3 a, b** and **Supplementary Figs. 42 and 43**). To aid assignment of the peaks in the PDFs, the published structures for the crystalline samples were refined using the PDF data, and weighted partial pair distributions $g_{ij}(r)$ calculated (**Supplementary methods**, **Supplementary Figs. 44-49**).

Peaks in the $D(r)$ for the crystalline samples at r = ~1.3 Å contain contributions from both from C–C, C–N (including C≡N) atom pairs, whilst the peak at r = 2.05 – 2.25 Å is ascribed predominantly to the M–N correlation (**Fig. 3a, Supplementary Figs. 42 and 43**). The movement of this peak to lower r, from Mn–N to Fe–N and to Co–N agrees well with the experimentally reported M–N distances. The strongest contribution to the peak at r = ~8.2 Å is primarily from the M-M distance in each case.

As expected, high r peaks broaden and weaken upon melt quenching in each case (**Fig. 3b, Supplementary Figs. 42, 43**). Nevertheless, the (now broad) peak centered around r = ~8.2 Å is the highest-r feature in $D(r)$ for each glass, and would therefore be consistent with the retention of some M-dca-M linkages. The broadening of peaks below 2 Å may arise as the result of partial decomposition, and decoordination of dca linkers is also evidenced. For example, the peak at 3.3 Å,

which mainly arises from the M–N–C correlation, appears to split into two peaks in the glass in each case. A partial splitting/broadening is also observed in the peak at 4.7 Å, which contains overlapping contributions from the M-N, M-C and C-C correlations.

First-principles molecular dynamics (FPMD) simulations were then employed, in order to characterize the microscopic evolution of [TPrA][Mn(dca)$_3$] upon melting (**Fig. 3c-e**). The dynamic nature of bond breaking prevented the use of classical force fields, and so FPMD simulations based on a quantum chemical description of the system at the density functional theory (DFT) level were chosen (**see methods**). Four separate MD simulations were performed on the crystalline material, at 300, 750, 1200, and 1700 K. Structural, dynamical, and thermodynamic properties were analysed along each trajectory. We note that most of these temperatures are far above the experimental ones as simulations describing bond breaking close to T_m would require simulations on the (impractical) microsecond timescale.

The PDFs at each temperature were calculated, and show the expected significant thermal broadening for Mn–N distances, in addition to the loss of long-range order (r > 6 Å) at the higher temperatures (**Fig. 3c**). The generalized Lindemann ratio was calculated for the Mn–N peak width, and found to exceed the Lindemann ratio between 750 and 1200 K (**Supplementary Table 4**).[31] Analysis of the N–Mn–N angles also confirm increased thermal fluctuations of the perfect octahedral environment upon heating (**Supplementary Fig. 50**), with broadening of the N–Mn–N bond angle peak centered at 90°. Analysis of the mean square displacement of [TPrA][Mn(dca)$_3$] over time (**Fig. 3e**) confirmed the liquid-like nature of the resulting melt, with a transition from restricted motion (less than 1 Å^2) resulting from framework vibrations at 300 K, to diffusive behaviour at 750 K and higher temperatures.

Observation of the trajectories revealed breaking and reformation of Mn–N bonds in the liquid state, in addition to significant movement of the propyl groups of the TPrA cations, starting at 1200 K. A series of free energy profiles from the Mn–N PDFs was therefore calculated (**Fig. 3d**). These potentials of mean force, i.e. $F(r) = -kT \ln g(r)$, are expressed as a function of the Mn–N distance, and reveal reduction in the

number of six-coordinated Mn atoms upon Mn-N bond breaking, i.e. analogous to coordination reduction observed in melting in ZIFs (**Supplementary Fig. 51**).[14]

From these data, we were able to fit the concentration, n_d, of five-coordinated M^{2+} ions, considered as a "defect" in the structure, with $n_d \propto \exp(-\Delta_f H_d / RT)$ and estimate an enthalpy for formation of $\Delta_f H_d$ ~ 91 kJ/mol (estimated between 1200 K and 1700 K). The value of the free energy barrier to melting (**Fig. 3d**) was estimated as ~ 85 kJ mol^{-1} at 1200 K, i.e. similar to other framework materials.[14] This significant barrier confirms that, as in conventional solids, melting occurs through a rare barrier-crossing event. However, in contrast with the case of porous MOFs, where this barrier is strongly-temperature dependent, here the impact of temperature is smaller; meaning the activation entropy involved is lower. We link this to the higher metal node coordination number of the materials here compared to ZIFs.

Electrical and Thermal Conductivity

Frequency dependent electrical conductivity measurements were carried out to probe the charge-transport behaviour of the a_g[TPrA][M(dca)$_3$] samples, and values of the in-phase AC impedance (Z') plotted with the corresponding out of phase component (Z'') (**Fig. 4a-c**). Values of DC–resistances (DC-R) were evaluated after fitting of the semicircular Nyquist plot. We ascribe the low frequency dispersion as the result of electrode polarization occurring when the material is subjected to an oscillating electric field.[32] Room temperature DC conductivities (σ_{RT}) of 0.02 x 10^{-4} S m^{-1}, 2.5 x 10^{-3} S m^{-1} and 0.66 x 10^{-4} S m^{-1} for the Mn, Fe and Co based glasses characterize these as moderately conducting materials (**Table 2**). All conductivities are however orders of magnitude larger than for the corresponding crystalline frameworks, (0.09 x 10^{-5} S m^{-1}, 0.64 x 10^{-5} S m^{-1} and 0.09 x 10^{-5} S m^{-1} respectively, **Supplementary Fig. 52**). We therefore postulate a mechanism of inter- or intra-chain hopping, involving the delocalized electron pair of the dca linker. Such a mechanism would be consistent with the increase in conductivity for the glasses, where the dca linker movement may be less constrained.[33]

The thermal conductivity of glasses is also of great importance given the applications of inorganics in e.g. thermoelectric materials[34] for waste-heat power generation and solid-state Peltier coolers.[35] The heat conductivity of a_g[TPrA][M(dca)$_3$] series was

probed, finding absolute values of thermal conductivity at room temperature (κ_{RT}) of 0.258 W m^{-1} K^{-1} for a_g[TPrA][Mn(dca)$_3$], 0.234 W m^{-1} K^{-1} for a_g[TPrA][Fe(dca)$_3$] and 0.228 W m^{-1} K^{-1} for a_g[TPrA][Co(dca)$_3$] (**Fig. 4d, Supplementary Fig. 53**). The similar values, despite the difference in M(0) content, suggests that the thermal insulating organic component predominates over the thermal conductive metallic components. These values are lower than the recently reported lead-halide perovskites (~ 0.40 - 0.50 W m^{-1} K^{-1}),[36,37] cobalt formate perovskite (~ 1.3 W m^{-1} K^{-1} [38]), Zn-MOF-5 (~ 0.32 W m^{-1} K^{-1} [39]) and ZIF-8 thin films (~ 0.33 W m^{-1} K^{-1} [40]) systems. They are also significantly less in comparison to other glass architectures, e.g. doped silicates or borosilicates (~ 1 W m^{-1} K^{-1}).[41]

Discussion

The relatively low melting points of the HOIPs (T_m ~ 250 °C) are in accordance with their substantially lower enthalpies of fusion ΔH_f (~ 46 - 65 kJ mol^{-1} ; **Fig. 1b**, **Table 1**) compared to other materials such as conventional quartz-silica (~ 911 kJ mol^{-1}).[42] This, alongside low activation energies, E_a, for the glass transition, point to a greater accessibility and processability of the liquid state compared to inorganics and ZIF-glasses.

The similarity of the melting mechanism, i.e. the rare event of metal-linker bond breakage, to that observed in inorganic solids and ZIFs, is in accordance with both Lindemann's Law and the dominant route to glass-formation being the quenching of the liquid state.[43,44] Some metal reduction and dca decomposition may explain the absence of glass recrystallisation, whilst the glass densities are notably also substantially higher than existing ZIF glasses,[45] though are still coupled to similar values of the Young's modulus (E ~ 6-7 GPa, **Table 2**, **Methods**, **Supplementary Fig. 56**). This points toward the dominant role of coordination bonding in determining the intermediate compliance of both MOF- and hybrid perovskite-derived glasses between organics and inorganics (**Fig**. **5a**).[18]

The glasses are set aside from existing coordination polymer glasses by their chemical tunability, alongside a range of potentially useful properties. These include moderate electrical conductivities at room temperature (10^{-3} -10^{-5} S m^{-1}), which are twice as large as those of various cation doped inorganic ion-conducting silicate,

borosilicate,[46] and also ZIF based glasses (e.g. a_gZIF-62(Co) ~ 0.8 x 10^{-6} S m^{-1}, **Supplementary Fig. 57**). They are also much larger than the electrical conductivity of the semiconductor lead halide perovskites (8.0 x 10^{-6} S m^{-1}).[37] Coupled with their very low values of thermal conductivity at room temperature (~ 0.2 W m^{-1} K^{-1}), which are also much lower than those in chemically similar ZIF glasses (e.g. a_gZIF-62(Co) ~ 2.7 W m^{-1} K^{-1}, **Supplementary Fig. 57**), these properties may suggest possible uses in thermoelectric settings such as efficient energy conversion and waste-heat power generation (**Fig. 5b**).[47]

The dca-containing family of perovskites themselves offer great potential for developing structure-property relationships by changing the '*A*' site ammonium cation, or by utilizing different transition metals on the '*B*' site(s), whilst the melting of HOIPs containing different organic linkers such as azides or hypophosphites will also be of interest.[7] This is in addition to studies of the effect of defects (near ubiquitous in the wider HOIP family) upon melting, and research into the interplay between metal reduction, ligand decomposition/rearrangement, recrystallisation and glass formation events. These studies may be key in raising electrical conductivities to approach those of the best inorganic (~ [10^3-10^6] S m^{-1})[48] and organic (~ [10^{-3}-10^5] S m^{-1})[49] thermoelectrics.

References

Acknowledgements

B.K.S. thanks the Royal Society and the Science and Engineering Research Board of India (SERB) for their combined support in Newton International Fellowship (NIF\R1\180163), T.D.B. the Royal Society for a University Research Fellowship (UF150021) and a research grant (RG94426), and the University of Canterbury Te Whare Wānanga o Waitaha, New Zealand, for a University of Cambridge Visiting Canterbury Fellowship. T.D.B. and L.N.M. also thank the Leverhulme Trust for a Philip Leverhulme Prize.

EPSRC is acknowledged for a Doctoral Training Studentship to A.R.H., a PhD studentship award under the industrial CASE scheme, along with Johnson Matthey PLC (JM11106) to A.F.S., and a PhD studentship award via the National Productivity Investment Fund (EP/R51231X/1) to A.P. M.D. and F.-X.C. acknowledge financial support from the Agence Nationale de la Recherche under the project "MATAREB" (ANR-18-CE29-0009-01) and access to high-performance computing platforms provided by GENCI grant A0070807069. A.D. acknowledges the DST-INSPIRE (IF160050), Government of India, for awarding his fellowship. S.K.S. gratefully thanks DST, Government of India, for the infrastructural facilities. B.K.S. acknowledges Robert Cornell (University of Cambridge) for his help to perform the dynamic-mechanical measurements. F.B. thanks Dr. Kevin J. Sanders (McMaster University) for assistance with the SHAPs pulses, and Dr. Konstantin Luzyanin (University of Liverpool) for collecting the liquid state NMR data. J. M. B.-G. acknowledges Xunta de Galicia for a Postdoctoral Fellowship. X. M. is grateful for support from the Royal Society. M.F.T would like to thank Corning Incorporated for project funding. We acknowledge the assistance of Louis Longley (University of Cambridge) in calorimetric data analysis. The authors gratefully acknowledge the provision of synchrotron access to Beamline I15-1 (EE20038), at the Diamond Light Source, Rutherford Appleton Laboratory, UK.

Author contributions

B.K.S. and T.D.B. designed the project. A.R.H., A. P. and F.B. performed all NMR experiments and analyzed the data. S.M. collected the HRMS data and analyzed them with F.B. B.K.S. and A.D. performed the electrical conductivity measurements. B.K.S. and S.K.S. analyzed the electrical conductivity data. T.D.B., A.F.S., M.F.T., L.N.M., D.A.K., D.S.K. and P.A.C. collected X-ray total scattering data. B.K.S., D.A.K., A.F.S. and T.D.B. analyzed the total scattering data. J.M.B. and X.M. aided the analysis and interpretation of calorimetric data. M.D. and F.-X.C. performed molecular simulations and analyzed the data. B.K.S. collected and analyzed all other data. All authors participated in manuscript writing, led by T.D.B and B.K.S.

Competing interests

The authors declare no competing interests.

Figure Legends

Figure 1. **Glass formation from hybrid perovskites**. **a**, Simplified representation of the [TPrA][Mn(dca)$_3$] structure at room temperature. Mn, C and N atoms are shown as pink, grey and blue spheres, respectively. All H atoms have been omitted for clarity, as have all TPrA ions except that located on the body-centre position. Furthermore, only one of the possible orientations of the TPrA and dca ions within the average crystal structure are shown.[8] **b**, Change in heat flow with increase in temperature for [TPrA][M(dca)$_3$] samples. Values for the enthalpy of fusion (ΔH_f) for the crystalline to liquid transition were extracted from the shaded sigmoidal areas, which were determined after subtracting sigmoidal baselines from the calorimetric data. Inset. Optical images of [TPrA][Mn(dca)$_3$] before heating (left) and after cooling (right). **c**, **(i) – (iii)** Variation of the average coefficient of linear thermal expansion (α) are shown with temperature for the glasses (a_g[TPrA][M(dca)$_3$]). Sudden drops in α indicate the T_f point in each case (**Supplementary Figure 9**). **d**, **(i) – (iii)** Variation of the loss modulus as a function of temperature for a_g[TPrA][M(dca)$_3$], obtained from dynamic mechanical analysis at 1 Hz. Glass transition temperatures (T_g) are determined from peak values and given in **Table 1**.

Figure 2. Structural insights into melting and glass structure. ^{13}C Double adiabatic echo MAS NMR spectra of crystalline [TPrA][Mn(dca)$_3$] before heating (pale green), after melt-quenching (green), crystalline [TPrA][Fe(dca)$_3$] (pale red), after melt-quenching (red), crystalline [TPrA][Co(dca)$_3$] before heating (pale blue) and after melt-quenching (blue). Magnified views of the 200 to -100 ppm

region (within box) are shown on the right hand side with spectral assignments. Spectra were processed with exponential line broadenings (of 20 Hz), appropriate for the magnified views shown in order to capture the various spectral features, while the overlaid views in the 6000 to 1000 ppm paramagnetic shifts region show data processed with increased line broadenings (of 200 Hz) taking into account the larger linewidths of the N*C*N resonances of the dca ligand. $C_3H_3N_3$ corresponds to triazine-based structures. Asterisks (*) denote spinning sidebands.

Figure 3. Pair Distribution Function Analysis. a, PDFs of [TPrA][Fe(dca)$_3$] and the corresponding glass a_g[TPrA][Fe(dca)$_3$]. **b**, PDFs of a_g[TPrA][Fe(dca)$_3$], a_g[TPrA][Co(dca)$_3$] and a_g[TPrA][Mn(dca)$_3$]. **c**, Evolution of the partial radial distribution function $g_{ij}(r)$ for Mn–N distances in [TPrA][Mn(dca)$_3$] at temperatures going from 300 K (navy blue) to 1700 K (red), from first principles molecular dynamics (FPMD). **d**, Potential of mean force $F(r)$ along the N–Mn distance coordinate at different temperatures. The discontinuities of some of the data arise from $F(r)$ being ill-defined null values of $g_{Mn\text{-}N}(r)$. Data from FPMD. **e**, Mean square displacement as a function of time MSD(t) for [TPrA][Mn(dca)$_3$], for temperatures ranging from 300 K (navy blue) to 1700 K (red). Data from FPMD.

Figure 4. Physical properties of melt-quenched glasses. Nyquist plot of real (Z') and imaginary (Z'') parts of frequency-dependent impedance for **a**, a_g[TPrA][Mn(dca)$_3$], **b**, a_g[TPrA][Fe(dca)$_3$], **c**, a_g[TPrA][Co(dca)$_3$] at 300 K. The cut-off point of the fitted theoretical line (black) at the x-axis gives the value of the DC-resistance. Low frequency (i.e. data points furthest from the origin) dispersion occurs due to electrode polarization. **d**, Logarithmic variation of thermal conductivity (κ) as a function of temperature for a_g[TPrA][M(dca)$_3$] from 2 to 300 K.

Figure 5. Comparison of physical properties of melt-quenched glasses with various materials. **a**, An Ashby plot of Young's modulus (E) vs. thermal expansion coefficient (α). Representative values of α were calculated from the data in Fig. 1c. **b**, An Ashby plot of thermal conductivity (κ) vs. electrical conductivity (σ) at 300 K. Both **a** and **b** show the comparison of glasses with various classes of materials including other glass types (blue font). Data in Ashby plots collated using the CES edupack software.[50]

Tables

Table 1. Physical properties of solid-liquid transitions in hybrid perovskites.[a]

Samples	T_m (°C)	ΔH_f (J g^{-1})	T_g – DSC (°C)	TMA (°C)	DMA – Onset of Storage Modulus (°C)	DMA – Peak of Loss Modulus (°C)	E_a (kJ mol^{-1})
[TPrA][Mn(dca)$_3$]	271	106.8	223	209	183	185	21.8
[TPrA][Fe(dca)$_3$]	263	118.8	225	220	213	219	12.2
[TPrA][Co(dca)$_3$]	230	147.8	125	102	146	145	20.6

[a] Errors associated with determination of T_g are typically up to 2 °C from DSC and 10-20 °C from DMA.[51]

Table 2: Physical properties of melt-quenched glasses.

Samples	*E* (GPa)	ρ_c (g cm^{-3})	ρ_g (g cm^{-3})	$\Delta\rho/\rho_g$	σ_{RT} x 10^{-4} (S m^{-1})	ε' at 2 MHz (tan δ)	κ_{RT} (W m^{-1}K^{-1})
a_g[TPrA][Mn(dca)$_3$]	6.65	1.237	1.335	0.073	0.02	32 (0.03)	0.258
	(±0.08)	(±0.005)	(±0.006)	(±0.005)			
a_g[TPrA][Fe(dca)$_3$]	5.85	1.225	1.326	0.076	25.0	-[a]	0.234
	(±0.09)	(±0.004)	(±0.002)	(±0.003)			
a_g[TPrA][Co(dca)$_3$]	6.98	1.245	1.283	0.030	0.66	30 (0.07)	0.228
	(±0.07)	(±0.005)	(±0.004)	(±0.004)			

[a] Unsaturated at the limit of the instrumental frequency, 2 MHz. Details of dielectric permittivity values can be found in the supplementary methods, and **Supplementary Figs. 54 and 55.**

References

1 Mitzi, D. B. Introduction: Perovskites. *Chem. Rev.* **119**, 3033-3035 (2019).

2 Li, W. *et al.* Chemically diverse and multifunctional hybrid organic-inorganic perovskites. *Nat. Rev. Mater.* **2**, 16099 (2017).

3 Li, W., Stroppa, A., Wang, Z.-M. & Gao, S. *Hybrid Organic-Inorganic Perovskites*. (Wiley, 2020).

4 Burschka, J. *et al.* Sequential deposition as a route to high-performance perovskite-sensitized solar cells. *Nature* **499**, 316-319 (2013).

5 Lee, M. M. *et al.* Efficient Hybrid Solar Cells Based on Meso-Superstructured Organometal Halide Perovskites. *Science* **338**, 643-647 (2012).

6 Jain, P. *et al.* Multiferroic Behavior Associated with an Order-Disorder Hydrogen Bonding Transition in Metal-Organic Frameworks (MOFs) with the Perovskite ABX(3) Architecture. *J. Am. Chem. Soc.* **131**, 13625-13627 (2009).

7 Wu, Y. *et al.* [Am]Mn(H2POO)(3): A New Family of Hybrid Perovskites Based on the Hypophosphite Ligand. *J. Am. Chem. Soc.* **139**, 16999-17002 (2017).

8 Bermudez-Garcia, J. M. *et al.* Role of Temperature and Pressure on the Multisensitive Multiferroic Dicyanamide Framework [TPrA][Mn(dca)(3)] with Perovskite-like Structure. *Inorg. Chem.* **54**, 11680-11687 (2015).

9 Saparov, B. & Mitzi, D. B. Organic-Inorganic Perovskites: Structural Versatility for Functional Materials Design. *Chem. Rev.* **116**, 4558-4596 (2016).

10 Egger, D. A., Rappe, A. M. & Kronik, L. Hybrid Organic-Inorganic Perovskites on the Move. *Acc Chem Res* **49**, 573-581 (2016).

11 Wang, Y. H. *et al.* Pressure-Induced Phase Transformation, Reversible Amorphization, and Anomalous Visible Light Response in Organolead Bromide Perovskite. *J. Am. Chem. Soc.* **137**, 11144-11149 (2015).

12 Ou, T. J. *et al.* Visible light response, electrical transport, and amorphization in compressed organolead iodine perovskites. *Nanoscale* **8**, 11426-11431 (2016).

13 Mitzi, D. B. Synthesis, crystal structure, and optical and thermal properties of (C4H9NH3)(2)MI(4) (M=Ge, Sn, Pb). *Chem. Mater.* **8**, 791-800 (1996).

14 Gaillac, R. *et al.* Liquid Metal-Organic Frameworks. *Nat. Mater.* **16**, 1149-1154 (2017).
15 Bermudez-Garcia, J. M. *et al.* Multiple phase and dielectric transitions on a novel multi-sensitive [TPrA][M(dca)(3)] (M: Fe2+, Co2+ and Ni2+) hybrid inorganic-organic perovskite family. *J. Mater. Chem. C* **4**, 4889-4898 (2016).
16 Umeyama, D. *et al.* Reversible Solid-to-Liquid Phase Transition of Coordination Polymer Crystals. *J. Am. Chem. Soc.* **137**, 864-870 (2015).
17 Bermudez-Garcia, J. M. *et al.* A simple in situ synthesis of magnetic M@CNTs by thermolysis of the hybrid perovskite [TPrA][M(dca)(3)]. *New. J. Chem.* **41**, 3124-3133 (2017).
18 Qiao, A. *et al.* A metal-organic framework with ultrahigh glass-forming ability. *Sci. Adv.* **4**, eaao6827 (2018).
19 Pell, A. J., Pintacuda, G. & Grey, C. P. Paramagnetic NMR in solution and the solid state. *Prog. Nucl. Mag. Res. Sp.* **111**, 1-271 (2019).
20 Ishii, Y., Wickramasinghe, N. P. & Chimon, S. A new approach in 1D and 2D C-13 high-resolution solid-state NMR spectroscopy of paramagnetic organometallic complexes by very fast magic-angle spinning. *J. Am. Chem. Soc.* **125**, 3438-3439 (2003).
21 Kervern, G., Pintacuda, G. & Emsley, L. Fast adiabatic pulses for solid-state NMR of paramagnetic systems. *Chem. Phys. Lett.* **435**, 157-162 (2007).
22 Gougeon, R. *et al.* High-resolution solid-state nuclear magnetic resonance study of the tetrapropylammonium template in a purely siliceous MFI-type zeolite. *Magn. Reson. Chem.* **36**, 415-421 (1998).
23 Hing, A. W., Vega, S. & Schaefer, J. Transferred-Echo Double-Resonance Nmr. *J. Mag. Res.* **96**, 205-209 (1992).
24 Tucker, M. C. *et al.* Hyperfine fields at the Li site in LiFePO4-type olivine materials for lithium rechargeable batteries: A Li-7 MAS NMR and SQUID study. *J. Am. Chem. Soc.* **124**, 3832-3833 (2002).
25 Tauber, K., Dani, A. & Yuan, J. Y. Covalent Cross-Linking of Porous Poly(ionic liquid) Membrane via a Triazine Network. *Acs Macro. Lett.* **6**, 1-5 (2017).
26 Kroke, E. *et al.* Tri-s-triazine derivatives. Part I. From trichloro-tri-s-triazine to graphitic C3N4 structures. *New. J. Chem.* **26**, 508-512 (2002).
27 Silverstein, R. M., Webster, F. X., Kiemle, D. J. & Bryce, D. L. *Spectrometric Identification of Organic Compounds 8th Edition*. (Wiley, 2014).
28 Orgel, L. E. Spectra of Transition-Metal Complexes. *J. Chem. Phys.* **23**, 1004-1014 (1955).
29 Bo, S. H. *et al.* Thin-Film and Bulk Investigations of LiCoBO3 as a Li-Ion Battery Cathode. *Acs Appl. Mater. Inter.* **6**, 10840-10848 (2014).
30 Schlueter, J. A., Manson, J. L. & Geiser, U. Structural and magnetic diversity in tetraalkylammonium salts of anionic M[N(CN)(2)](3)(-) (M = Mn and Ni) three-dimensional coordination polymers. *Inorg. Chem.* **44**, 3194-3202 (2005).
31 Chakravarty, C., Debenedetti, P. G. & Stillinger, F. H. Lindemann measures for the solid-liquid phase transition. *J. Chem. Phys.* **126**, 204508 (2007).
32 Leo, C. J., Rao, G. V. S. & Chowdari, B. V. R. Fast ion conduction in the Li-analogues of Nasicon, Li1+x [(Ta1-x Ge-x)Al](PO4)(3). *J. Mater. Chem.* **12**, 1848-1853 (2002).
33 Chowdari, B. V. R., Yoo, H.-L., Choi, G. M. & Lee, J.-H. *Solid State Ionics: the Science and Technology of Ions in Motion*. (World Scientific, 2004).
34 Snyder, G. J. & Toberer, E. S. Complex thermoelectric materials. *Nat. Mater.* **7**, 105-114 (2008).
35 Bell, L. E. Cooling, heating, generating power, and recovering waste heat with thermoelectric systems. *Science* **321**, 1457-1461 (2008).
36 Pisoni, A. *et al.* Ultra-Low Thermal Conductivity in Organic-Inorganic Hybrid Perovskite CH3NH3PbI3. *J. Phys. Chem. Lett.* **5**, 2488-2492 (2014).

37 Ye, T. *et al.* Ultra-high Seebeck coefficient and low thermal conductivity of a centimeter-sized perovskite single crystal acquired by a modified fast growth method. *J. Mater. Chem. C* **5**, 1255-1260 (2017).
38 Gunatilleke, W. D. C. B. *et al.* Thermal conductivity of a perovskite-type metal-organic framework crystal. *Dalton Transactions* **46**, 13342-13344 (2017).
39 Huang, B. L. *et al.* Thermal conductivity of a metal-organic framework (MOF-5): Part II. Measurement. *Int. J. Heat. Mass Tran.* **50**, 405-411 (2007).
40 Cui, B. Y. *et al.* Thermal Conductivity of ZIF-8 Thin-Film under Ambient Gas Pressure. *Acs Appl. Mater. Inter.* **9**, 28139-28143 (2017).
41 Bansal, N. P. & Doremus, R. H. *Thermal Conductivity*. (Elsevier, 1986).
42 Richet, P. Viscosity and Configurational Entropy of Silicate Melts. *Geochim. Cosmochim. Ac.* **48**, 471-483 (1984).
43 Debenedetti, P. G. & Stillinger, F. H. Supercooled liquids and the glass transition. *Nature* **410**, 259-267 (2001).
44 Angell, C. A. Formation of Glasses from Liquids and Biopolymers. *Science* **267**, 1924-1935 (1995).
45 Bennett, T. D. *et al.* Melt-Quenched Glasses of Metal-Organic Frameworks. *J. Am. Chem. Soc.* **138**, 3484-3492 (2016).
46 Bansal, N. P. & Doremus, R. H. *Electrical Conductivity*. (Elsevier, 1986).
47 Wu, Y. *et al.* Hypophosphite hybrid perovskites: a platform for unconventional tilts and shifts. *Chem. Commun.* **54**, 3751-3754 (2018).
48 Gaultois, M. W. *et al.* Data-Driven Review of Thermoelectric Materials: Performance and Resource Considerations. *Chem. Mater.* **25**, 2911-2920 (2013).
49 Russ, B. *et al.* Organic thermoelectric materials for energy harvesting and temperature control. *Nat. Rev. Mater.* **1**, 16050 (2016).
50 CES Edupack 2019 software (Granta Design Ltd, Cambridge, 2019).
51 Menard, K. P. & Menard, N. R. in *Encyclopedia of Polymer Science and Technology* 1-33 (Wiley, 2015).

Methods

Synthesis of Hybrid Perovskites

Reagents: $Mn(NO_3)_2.4H_2O$ (98.5%, Sigma-Aldrich), $FeCl_2.4H_2O$ (98%, Sigma-Aldrich), $Co(NO_3)_2.6H_2O$ (98%, Sigma-Aldrich), (TPrA)Br (98%, Aldrich), Na(dca) (96%, Sigma-Aldrich), Imidazole (99%, Sigma-Aldrich), Benzimidazole (98%, Sigma-Aldrich) and N,N-dimethylformamide (99.8%, Fisher Chemical). were purchased as indicated and used as received.

Procedure: The synthesis reported in the literature was followed.[8,15,30] Specifically, 10 mL of an aqueous solution of metal (Mn^{2+}, Fe^{2+}, Co^{2+}), (2 mmol) was placed at the bottom of a thin crystallization tube and layered with a mixture of a solution of Na(dca) (6 mmol in 10 mL of water) and (TPrA)Br (2 mmol in 10 mL of ethanol). Block-shaped single crystals were obtained from the mother liquor after one week of slow evaporation in an open atmosphere, and are colourless (Mn), pale yellow (Fe) and pink (Co) respectively.

We note that the Fe(II) and Co(II) analogues each exhibit three first-order structural phase transitions, arising from a displacement of TPrA cations and order-disorder transitions of both TPrA cations and dca anions. The Mn(II) analogue shows type-I multiferroism,[8] due to coexistence of antiferroelectric (AFE) and antiferromagnetic (AFM) order. A high sensitivity to applied external pressure facilitates a giant caloric effect of 37.0 J kg^{-1} K^{-1}.[52] This occurs under very low applied pressures (P < 7 MPa), just above room temperature, with a calculated barocaloric tunability ($\partial T_t/\partial P$) of 23.1 K $kbar^{-1}$.[52,53]

Synthesis of Zeolitic Imidazolate Framework Glass

The method previously reported by Henke *et al.* was used here.[54] Specifically, $Co(NO_3)_2 \cdot 6H_2O$ (4.0 mmol, 1.2 g) and a mixture of 7 eq. imidazole (Him; 0.786 g, 11.55 mmol) and 1 eq. benzimidazole (Hbim; 0.196 mg, 1.66 mmol) were dissolved in 90 mL N,N-dimethylformamide (DMF). The obtained solution was divided in ten 9 mL portions, which were transferred into ten 12 mL borosilicate glass vials. The tightly sealed reaction vials were transferred to a preheated oven (at 130 °C) for 7 days. After cooling to room temperature, the reaction volumes were recombined, filtered and washed three times with 20 mL DMF. Deep purple ZIF-62(Co) crystals were obtained as large, truncated octahedrally shaped single crystals. The as-synthesized material was dried at 200 °C under dynamic vacuum (p ~ 10^{-3} mbar) for 20 h to evacuate the sample. This sample was then ground by hand, before heating in the DSC to 475 °C under Argon atmosphere at a heating rate 10 °C min^{-1}. The liquid formed was then cooled to room temperature (cooling rate 10 °C min^{-1}) to obtain the glass.

Thermal Analysis

Thermogravimetric analysis (TGA) was carried out in a SDT-Q600 apparatus (TA Instruments). Data were collected in the range from 25 ºC to 400 ºC at a scan rate of 10 ºC min^{-1} under an Argon atmosphere.

Differential Scanning Calorimetry (DSC) measurements were conducted using a Netzsch 214 Polyma instrument. Samples were hand-ground, placed in an aluminum pan and heated up to their respective melting offset at a heating rate of 10 ºC min^{-1} under Argon atmosphere. To obtain the glass transition, the melted solids were cooled to 60 °C at 10 ºC min^{-1}, and then reheated at 10 ºC min^{-1} up to the targeted temperature.

Simultaneous DSC-TGA (SDT) measurements were conducted using a TA Q600 instrument, under Argon flow at a heating rate 10 ºC min^{-1}. ~ 10 mg of ground sample was placed into a 70 µL Alumina crucible in each case.

Preparation of Glasses in DSC and SDT Measurements

a_g[TPrA][$Mn(dca)_3$]: A ground sample of [TPrA][$Mn(dca)_3$] was heated at 10 ºC min^{-1} to 277 ºC, then cooled under an Argon atmosphere (100 ml/min flow rate), before cooling back to room temperature at ca. 3 ºC min^{-1}. Samples formed in the SDT instrument were used for NMR, XPS, HR-MS, FT-IR, and PDF measurements.

a_g[TPrA][Fe(dca)$_3$]: Crystals of [TPrA][Fe(dca)$_3$] were cooled from 269 ºC, under an Argon atmosphere (100 ml/min flow rate), at a rate of ca. 10 ºC min^{-1}. Samples formed in the SDT instrument were used for NMR, XPS, HR-MS, FT-IR, and PDF measurements.

a_g[TPrA][Co(dca)$_3$]: A ground sample of [TPrA][Co(dca)$_3$] was rapidly cooled from 264 ºC, under an Argon atmosphere. A cooling rate of ca. 30 ºC min^{-1} was used, i.e. the cooling rate attained by the instrument on cooling back to room temperature without a given ramp rate. Samples formed in the DSC instrument were used for NMR, XPS, HR-MS, FT-IR, and PDF measurements.

In the cases of a_g[TPrA][Mn(dca)$_3$] and a_g[TPrA][Fe(dca)$_3$], partial recrystallisation was observed upon cooling the melt from 263 ºC and 271 ºC respectively, indicating the complex interplay between decomposition, recrystallisation and vitrification (**Supplementary Fig. 6**).

Thermomechanical analysis

For a_g[TPrA][Mn(dca)$_3$] and a_g[TPrA][Fe(dca)$_3$], dense flat pieces of quenched-glass samples were used to determine the CTE and T_f values, however due to the irregular shape of the a_g[TPrA][Co(dca)$_3$], a pelletized glass sample was used. In this technique, the linear expansion of the glasses is measured as a function of temperature at a standard TMA heating rate of 5 ºC min^{-1} with a standard applied force of 10 mN by means of a dilatometer under N_2 atmosphere in TMA-Q400 apparatus (TA Instruments).

Dynamic mechanical analysis

Glass transition relaxation dynamics were investigated using a TA instruments dynamic mechanical analyzer, DMA-Q800 (**Supplementary Fig. 58**). To perform the measurements, amorphous powders were wrapped in an aluminum foil, in a rectangular sample geometry. The sample geometry was pre-calibrated with polycarbonate reference. Well-prepared specimens of equal masses and of even thickness (dimension of ~ 35.0 mm x 12.8 mm x 3.2 mm) in parallel sides are finally placed in single cantilever. A slow heating rate of 2 ºC min^{-1} is applied to minimize the thermal fluctuation and dipolar coupling (low loss/heat dissipation) with an applied frequency varying from 1-3 Hz.

The out of phase component (loss modulus) and the loss (tan δ) reveal a strong broad peak close to the softening point. Broad peaks as witnessed here, have also been observed in DMA of other materials, such as highly cross-linked polymers. The loss modulus is considered more reliable for the accurate determination of T_g, due to the very low storage moduli of the glasses.[55]

Powder X-ray diffraction

Ambient Temperature: X-ray powder diffraction (PXRD) patterns were recorded (2θ = 10°– 60°) on a Bruker D8 Advance diffractometer (equipped with a LynxEye EX linear position sensitive detector) in Bragg-Brentano geometry using Cu Kα (λ = 1.540598 Å) source fitted with a Ni 0.012 mm filter. Data were collected in 2θ step size of 0.02°, with 10 s per step.

Scanning electron microscopy

The surface morphologies of the melt quenched glass samples were investigated using a high-resolution scanning electron microscope, FEI Nova Nano SEM 450, operated at 5 kV (working distance ~ 5.5 mm). Palladium sputtering was used to reduce charging of the specimen.

Nuclear magnetic resonance (NMR)

Solid State NMR: Solid state NMR experiments were performed on a 9.4 T Bruker Avance III HD spectrometer equipped with a 1.3 mm HXY magic angle spinning (MAS) probe in double resonance mode. All spectra were recorded under an optimised approach for paramagnetic systems combining very fast MAS[20] at a spinning rate of 60 kHz with double adiabatic echo detection and shaped pulses.[21]

Solid state NMR experiments were performed on a 9.4 T Bruker Avance III HD spectrometer equipped with a 1.3 mm HXY magic angle spinning (MAS) probe in double resonance mode. The ^{1}H channel was tuned to $\nu_0(^{1}H)$ = 400.13 MHz and the X channel was tuned to $\nu_0(^{13}C)$ = 100.61 MHz. Spectra were recorded under an optimised approach for paramagnetic systems combining very fast MAS[20] with double adiabatic echo detection and shaped pulses[21]. All NMR spectra were recorded at a spinning rate of 60 kHz, corresponding to a sample temperature of *ca.* 45 °C (as measured from the ^{79}Br NMR chemical shift change of KBr[56]), and pulses were applied at a radiofrequency field of 200 kHz at an offset of 0 ppm for [TPrA][Mn(dca)$_3$], and 2985 ppm for both [TPrA][Fe(dca)$_3$] and [TPrA][Co(dca)$_3$. The double adiabatic echo pulse sequence[18] was employed to record the MAS NMR spectra and used square $\pi/2$ excitation pulses of duration 1.25 μs and rotor synchronised short (50 μs) high powered adiabatic tanh/tan (SHAPs) inversion pulses sweeping through 10 MHz to refocus the chemical shift evolution[21]; this sequence shows an approximate two-fold increase in signal intensity versus the double echo pulse sequence employing square $\pi/2$ and π pulses, largely in agreement with the literature.[21] TEDOR experiments[21,23] were performed with an optimised recoupling time equal to 3 rotor periods (50 μs) and adiabatic SHAPs inversion pulses applied to the ^{1}H channel to improve polarization transfer.[24] TEDOR experiments were performed with a recycle delay of 1.3 x ^{1}H T_1 to ensure maximum signal to noise per unit time. No ^{1}H decoupling was used during any solid state NMR ^{13}C acquisition. The ^{13}C MAS NMR spectra were typically accumulated with 2 million scans with recycle delays of 0.01 s which were found to be long enough to avoid saturation. Note that the ^{13}C signal intensities do not directly relate to the number of carbons present as the optimised data acquisition strategy is not quantitative due to the likely large differences in the ^{13}C T_2' (transverse magnetization decay time constant with refocused inhomogeneous broadening) values. ^{1}H spectra were referenced to H_2O at 4.8 ppm and ^{13}C spectra were reference to the CH peak of adamantane at 29.45 ppm corresponding to TMS at 0 ppm.[57] All samples for solid state NMR were finely ground.

No ^{13}C resonance outside the standard diamagnetic 200 to 0 ppm region was observed in crystalline [TPrA][Mn(dca)$_3$] (**Supplementary Fig. 12**) prompting us to explore the use of ^{13}C-edited experiment to identify the dca carbon which is best achieved in these systems with a ^{1}H ^{13}C double resonance TEDOR NMR experiment.[21,23] In this experiment, only protonated carbons are observed and the corresponding ^{1}H-^{13}C TEDOR NMR spectrum of [TPrA][Mn(dca)$_3$] unambiguously showed the

disappearance of the 3-7 ppm signal which is therefore assigned to the carbon of the dca anion ligand.

The spectral deconvolution of [TPrA][Co(dca)$_3$] and [TPrA][Fe(dca)$_3$] in **Supplementary Figures 15** and **16** shows three resonances in the 200 to -100 ppm region corresponding to three carbon environments within the TPrA molecule in the unit cell.[15] The spectral deconvolution of [TPrA][Mn(dca)$_3$] in **Supplementary Figure 17** shows three resonances corresponding to the N***C***H$_2$ within the TPrA molecule and two resonances for the N***C***N at 7 and 3 ppm within the dca ligand in a 2:1 ratio. This is in agreement with the expected number of carbon environments in the unit cell for this compound.[8] The limited resolution does not permit the ***C***H$_2$CH$_3$ and ***C***H$_3$ groups to be distinguished from one another.

The NMR of the crystalline compounds are therefore consistent with their crystal structures.[8,15] Specifically, they support the existence of one TPrA cation and two dca anions in the asymmetric unit cell within the orthorhombic *Ibam* (centrosymmetric) space group of [TPrA][Fe(dca)$_3$] and [TPrA][Co(dca)$_3$],[15] and the presence of three independent ions in the tetragonal space group *P-42$_1$c* of [TPrA][Mn(dca)$_3$] at 45 °C.[8]

Liquid phase NMR: Experiments were performed on a 9.4 T Bruker Avance III HD spectrometer equipped with a 5 mm BBFO probe. NMR digested samples were prepared by dissolving ~8 mg in 100 µL of 35 wt% DCl in D_2O then dissolved in 500 µL of DMSO-d_6. Deuterium was used to remove ^{1}H signal from the solvent, though the D_2O still contained some H_2O.

Liquid phase NMR experiments were performed on a 9.4 T Bruker Avance III HD spectrometer equipped with a 5 mm BBFO probe. Digested samples were prepared by dissolving ~8 mg in 100 µL of 35 wt% DCl in D_2O then dissolved in 500 µL of DMSO-d_6. Deuterium was used to remove ^{1}H signal from the solvent, though the D_2O still contained some H_2O. Upon digestion of the ground samples, pink [TPrA][Co(dca)$_3$], off-white [TPrA][Mn(dca)$_3$] and yellow-ish / off-white [TPrA][Fe(dca)$_3$] change in solution to blue (likely corresponding to tetrahedral $[CoCl_4]^{2-}$), colourless and yellow, respectively. ^{1}H chemical shifts are reported relative to the corresponding signals of residual protons in DMSO-d_6 at 2.50 ppm. ^{13}C spectra were recorded with ^{1}H decoupling and are reported relative to the DMSO-d_6 signal at 39.50 ppm (the $^1J_{CD}$ = 21 Hz is not resolved in the Fe and Co samples as this signal is too broad). br indicated that signals are broad. The ^{1}H and ^{13}C spectra were recorded with 16 and 960-4000 scans, respectively.

Upon acidic sample digestion, decoordination of the TPrA and dca ligands readily occurs as evidenced by the ^{1}H and ^{13}C liquid phase NMR spectra (**Supplementary Figures 19-24**). These also present a range of broadening that depends on the strength of the paramagnetism which is largely a function of the hyperfine coupling to the paramagnetic ion. Starting with the most resolved NMR spectra for the crystalline and glass-quenched Co samples, the NMR spectra of the TPrA ligand are straightforward to assign based on chemical shifts and electron withdrawing of the nitrogen atoms. Some scalar J couplings are observed in the ^{1}H NMR spectra of both [TPrA][Co(dca)$_3$] and a_g[TPrA][Co(dca)$_3$]. Cyanamide exists as two aminonitrile – carbodiimide tautomers which for the dca

ligand translates into the equilibrium depicted in **Supplementary Scheme 1**. There the ^{1}H NMR spectra of both Co materials display a single resonance at *ca.* 8 ppm for the NH group that is likely in exchange between both tautomers at room temperature under acidic condition. The ^{13}C NMR spectrum of [TPrA][Co(dca)$_3$] shows two additional resonances to TPrA at around 150 and 110 ppm that can be attributed to the carbodiimide and nitrile carbons, respectively,[27] while only the later resonance is observed in a_9[TPrA][Co(dca)$_3$] (the signal of the nitrile carbon is likely in the noise level) that still undoubtedly demonstrates the presence of dca, further confirmed by HRMS data (below).

The ^{1}H NMR spectra of the Fe and Co samples are significantly broadened by hyperfine coupling (especially for Co^{2+}), however all four resonances for TPrA and the dca tautomers as described above are clearly observed indicating that the quenched-glass samples contain both ligands. Whilst the ^{13}C NMR spectrum of [TPrA][Fe(dca)$_3$] is virtually identical to the one of the corresponding Mn one, the signals arising from the dca ligand are just above the noise level. In the corresponding glasses, these are challenging to observe, despite extended experimental times, nevertheless the NH resonance in the more sensitive ^{1}H spectra conclusively confirm the presence of the dca ligand.

High Resolution Mass Spectrometry (HRMS)

HRMS data were record on an Agilent 6540A Quadrupole-Time-Of-Flight (TOF) mass spectrometer using Electrospray Ionisation (ESI) in negative or positive. Digested samples were prepared by dissolving ~1 mg of samples in acidic aqueous-methanol solutions.

Digested samples were prepared by dissolving ~1 mg of samples in 1 mL of either H_2O (with or without 50 μL of HCO_2H) or a H_2O:CH_3OH mixture in a 1:1 ratio (v/v) as indicated above to ensure dissolution. H_2O or a H_2O:CH_3OH mixture in a 8:2 ratio (v/v) (for the samples dissolved with CH_3OH), all containing 0.1% of HCO_2H, were used as the eluent.

m/z found in ESI$^-$ at 69.9961 and 112.9853 are trifluoromethane ion (calculated for [CF_3^-] 68.9952) and trifluoroacetic acid (calculated for [$CF_3CO_2^-$] 112.9850), respectively, as part of the set of reference ions used for HRMS were subtracted from the data for clarity.

Samples were digested in weakly acidic aqueous – methanolic condition to ensure full dissolution. **Supplementary Figures 25a-30a** provide the HRMS data using the ESI mode with positive ion detection and revealed a very strong and clear signal for the $[TPrA]^+$ molecular ion (m/z calculated 186.2222, found 186.2214-186.2222) in all crystalline and melt-quenched Mn, Fe and Co materials. The corresponding data for the negatively charged ions are given in **Supplementary Figures 25b-30b** and highlighted that the dca^- ion is present either as its molecular ion (m/z calculated 66.0092, found 66.0101-66.0104), an H_2O-adduct (m/z calculated 84.0198, found 84.0203-84.0206) or a $[Mn+3xdca]^-$ complex (m/z calculated 252.9657, found 252.9654). These HRMS data undoubtedly demonstrate that dca and TPrA species remain largely intact upon melting.

FT-IR study

Fourier-transform Infrared spectra were collected in Transmittance mode using a Bruker Tensor 27 spectrometer on grounded crystal, prior to melting and glass samples.

Diffuse reflectance UV-Vis study

A Perkin Elmer Lambda 750 spectrophotometer was used to measure the solid-state diffuse reflectance UV-Vis spectra. Spectra for all grounded crystalline and glass powder samples were recorded in the range of 200−800 nm. A $BaSO_4$ matrix was used as a reference. Absorbances were estimated using the Kubelka−Munk transform function αKM/s = (1 − R)2 /2R, where R is the measured diffuse reflectance and s is an unknown sample scattering coefficient.[58]

Magnetic study

A SQUID MPMS 3 instrument was used to conduct the magnetic measurements of hybrid perovskite crystals and glasses. The temperature variation of field-cooled susceptibility (*M*-*T*) data was collected at 500 Oe magnetic field at a temperature range 2 – 300 K. Magnetization as a function of magnetic field (*M*-*H*) was measured at temperature 300 K, with magnetic field varying up to 7 T. Samples were placed in a light weight homogeneous quartz tube to minimize the background noise and stray field effects. The magnetic data were corrected for the diamagnetic contribution from the quartz sample holder and the intrinsic diamagnetism of the samples by the standard literature using Pascal's constants.[59]

XPS spectroscopy

Ground powder samples of crystals and glasses were used to perform the measurements using Escalab 250Xi, monochromatic Al k Alpha x-ray source. An inert, UHV conditions were also applied.

X-ray total scattering experiments

X-ray data were collected at the I15-1 beamline at the Diamond Light Source, UK (λ = 0.161669 Å, 76.7 keV). Samples were loaded into borosilicate capillaries of 1.17 mm inner diameter. Data on the samples, empty instrument and capillary were collected in the region of ∼0.4 < Q <∼26 $Å^{-1}$. Corrections for background, multiple scattering, container scattering, Compton scattering, fluorescence and absorption were performed using the GudrunX program.[60,61]

Network density measurements

Physical densities of all hybrid perovskite crystals and glasses were measured using Micromeritics Accupyc 1340 helium pycnometer. The typical mass used for each test was around 80 mg. The reported values were averaged over a cycle of 10 measurements.

First-principles molecular dynamics

The behaviour of [TPrA][$Mn(dca)_3$] as a function of temperature was studied by means of density functional theory (DFT)-based molecular dynamics (MD) simulations, using the Quickstep module[62] of the CP2K software package (Available online at http://www.cp2k.org). The simulated configuration was the tetragonal crystallographic unit cell, which contains 456 atoms, with cell parameters $a = b =$ 16.275 Å, c = 17.423 Å, and $\alpha = \beta = \gamma = 90°$ (**Supplementary Methods, Results and Discussions**).

AC electrical conductivity measurements

Room temperature AC conductivity measurements were performed with an Agilent E4980A Precision LCR meter, capable to measure in the frequency range from 20 Hz up to 2 MHz (**Supplementary Methods, Results and Discussions**).

Thermal conductivity measurements

Thermal conductivities of the glasses were measured by Quantum Design's Physical Property Measurement System (DynaCool^{TM}) using the TTO mode (thermal transport option) in a two-probe lead configuration (**Supplementary Methods, Results and Discussions**, **Supplementary Fig. 59**).

Elemental characterization from CHN analysis

The elemental compositions were obtained from CHN analyzer (**Supplementary Table 3**). Compared to crystalline states, a minor decrease in the concentration of carbon (~0.4%) and nitrogen (~0.3%) was observed in the glasses. Ground powder samples were used to perform the measurements using CE440 Elemental Analyzer, EAI Exeter Analytical Inc.

Elemental characterization from SEM-EDX analysis

The percentage of N and M contents was evaluated for the glasses from SEM-EDX spectra (**Supplementary Fig. 60**, **Supplementary Table 3**). Nitrogen ratios were found to vary slightly in comparison to the XPS and CHN results. The spectra were recorded with a high energy electron beam ~ 10 keV.

Nanoindentation

Dense flat pieces of quenched-glass samples were mounted with epoxy resin and finely polished prior to Nanoindentation tests. A MTS Nanoindenter *XP* instrument was used under dynamic displacement controlled mode, at a constant strain rate of 0.05 s^{-1} at ambient conditions. Deformation of the polished samples was made using a Berkovich diamond tip, pre-calibrated with fused silica. A Poisson's ratio of v = 0.2 was used in accordance with prior literature.[45] Use of v = 0.34, as reported by Yue et al[63] led to changes in *E* of <1%. Absolute values of Young's modulus (*E*) were determined from the variable indentation depth scans to a maximum surface penetration of 1000 nm which are shown with error bars over 20 consecutive scans.

References for Methods Section

8 Bermudez-Garcia, J. M. *et al.* Role of Temperature and Pressure on the Multisensitive Multiferroic Dicyanamide Framework [TPrA][Mn(dca)(3)] with Perovskite-like Structure. *Inorg. Chem.* **54**, 11680-11687 (2015).

15 Bermudez-Garcia, J. M. *et al.* Multiple phase and dielectric transitions on a novel multi-sensitive [TPrA][M(dca)(3)] (M: Fe2+, Co2+ and Ni2+) hybrid inorganic-organic perovskite family. *J. Mater. Chem. C* **4**, 4889-4898 (2016).

20 Ishii, Y., Wickramasinghe, N. P. & Chimon, S. A new approach in 1D and 2D C-13 high-resolution solid-state NMR spectroscopy of paramagnetic organometallic complexes by very fast magic-angle spinning. *J. Am. Chem. Soc.* **125**, 3438-3439 (2003).
21 Kervern, G., Pintacuda, G. & Emsley, L. Fast adiabatic pulses for solid-state NMR of paramagnetic systems. *Chem. Phys. Lett.* **435**, 157-162 (2007).
23 Hing, A. W., Vega, S. & Schaefer, J. Transferred-Echo Double-Resonance Nmr. *J. Mag. Res.* **96**, 205-209 (1992).
24 Tucker, M. C. *et al.* Hyperfine fields at the Li site in LiFePO4-type olivine materials for lithium rechargeable batteries: A Li-7 MAS NMR and SQUID study. *J. Am. Chem. Soc.* **124**, 3832-3833 (2002).
27 Silverstein, R. M., Webster, F. X., Kiemle, D. J. & Bryce, D. L. *Spectrometric Identification of Organic Compounds 8th Edition*. (Wiley, 2014).
30 Schlueter, J. A., Manson, J. L. & Geiser, U. Structural and magnetic diversity in tetraalkylammonium salts of anionic M[N(CN)(2)](3)(-) (M = Mn and Ni) three-dimensional coordination polymers. *Inorg. Chem.* **44**, 3194-3202 (2005).
45 Bennett, T. D. *et al.* Melt-Quenched Glasses of Metal-Organic Frameworks. *J. Am. Chem. Soc.* **138**, 3484-3492 (2016).
52 Bermudez-Garcia, J. M. *et al.* Giant barocaloric tunability in [(CH3CH2CH2)(4)N]Cd[N(CN)(2)](3) hybrid perovskite. *J. Mater. Chem. C* **6**, 9867-9874 (2018).
53 Bermudez-Garcia, J. M. *et al.* Giant barocaloric effect in the ferroic organic-inorganic hybrid [TPrA][Mn(dca)(3)] perovskite under easily accessible pressures. *Nat. Commun.* **8**, 15715 (2017).
54 Frentzel-Beyme, L. *et al.* Porous purple glass - a cobalt imidazolate glass with accessible porosity from a meltable cobalt imidazolate framework. *J. Mat. Chem. A* **7**, 985-990 (2019).
55 Li, G., Lee-Sullivan, P. & Thring, R. W. Determination of activation energy for glass transition of an epoxy adhesive using dynamic mechanical analysis. *J. Therm. Anal. Calorim.* **60**, 377-390 (2000).
56 Thurber, K. R. & Tycko, R. Measurement of sample temperatures under magic-angle spinning from the chemical shift and spin-lattice relaxation rate of Br-79 in KBr powder. *J. Mag. Res.* **196**, 84-87 (2009).
57 Morcombe, C. R. & Zilm, K. W. Chemical shift referencing in MAS solid state NMR. *J. Mag. Res.* **162**, 479-486 (2003).
58 Fuller, M. P. & Griffiths, P. R. Diffuse Reflectance Measurements by Infrared Fourier-Transform Spectrometry. *Anal. Chem.* **50**, 1906-1910 (1978).
59 Bain, G. A. & Berry, J. F. Diamagnetic corrections and Pascal's constants. *J. Chem. Educ.* **85**, 532-536 (2008).
60 Soper, A. K. GudrunN and GudrunX: Programs for Correcting Raw Neutron and X-ray Diffraction Data to Differential Scattering Cross Section. *Tech. Rep. RAL-TR-2011-013* (2011).
61 Soper, A. K. & Barney, E. R. Extracting the pair distribution function from white-beam X-ray total scattering data. *J. Appl. Crystallogr.* **44**, 714-726 (2011).
62 VandeVondele, J. *et al.* QUICKSTEP: Fast and accurate density functional calculations using a mixed Gaussian and plane waves approach. *Comput. Phys. Commun.* **167**, 103-128 (2005).
63 To, T. *et al.* Fracture toughness of a metal-organic framework glass. *Nat. Commun.* **11** (2020).

Data availability

Representative input files for the molecular dynamics simulations are available as Supporting Information and online in our data repository at https://github.com/fxcoudert/citable-data. The experimental data that support the findings of this study are available in Symplectic Elements with the identifier(s): https://doi.org/10.17863/CAM.63032.

Code availability

The CP2K code is freely available at cp2k.org.

a

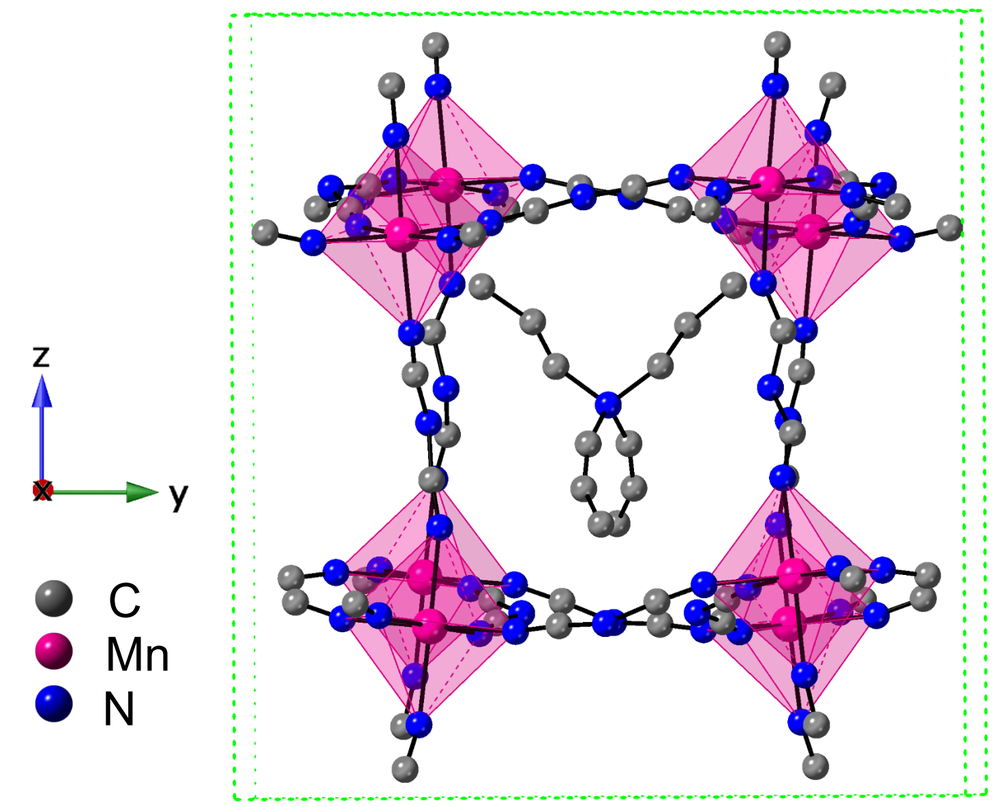
z
y
C
Mn
N

b

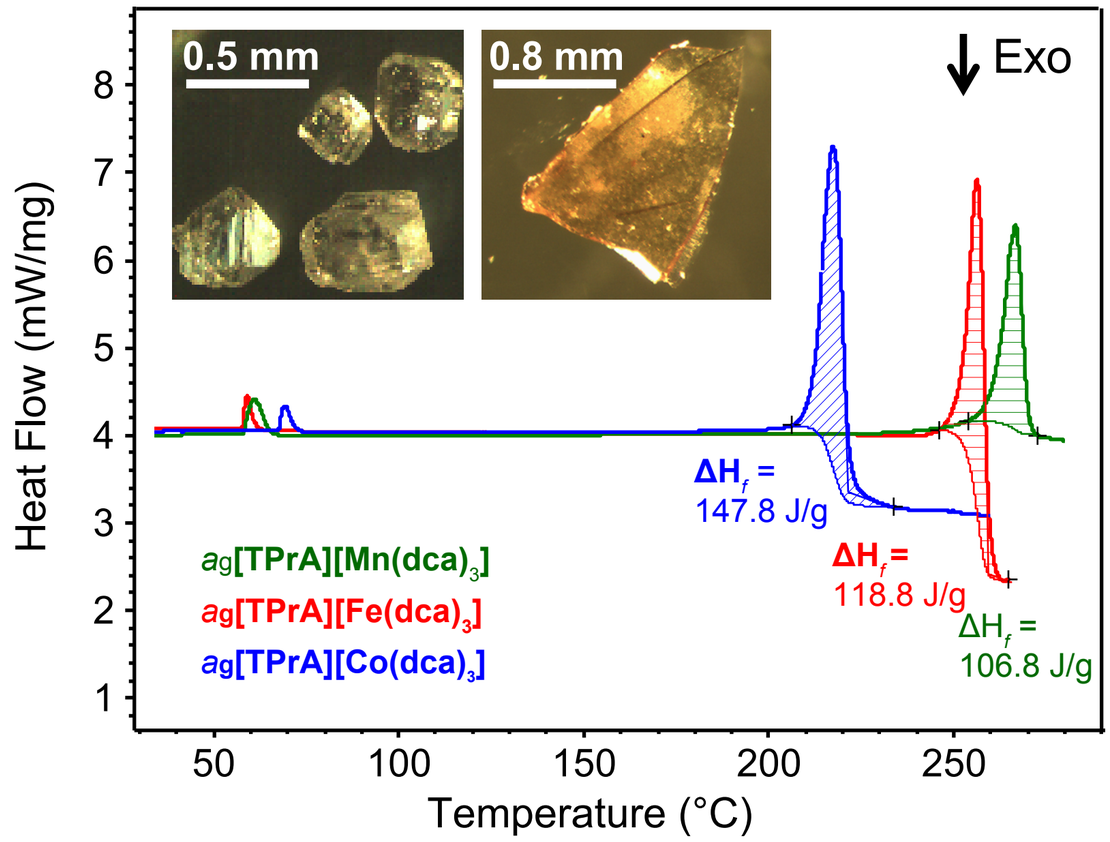
0.5 mm
0.8 mm
Exo
Heat Flow (mW/mg)
Temperature (°C)
ΔH_f = 147.8 J/g
ΔH_f = 118.8 J/g
ΔH_f = 106.8 J/g
ag[TPrA][Mn(dca)3]
ag[TPrA][Fe(dca)3]
ag[TPrA][Co(dca)3]

c

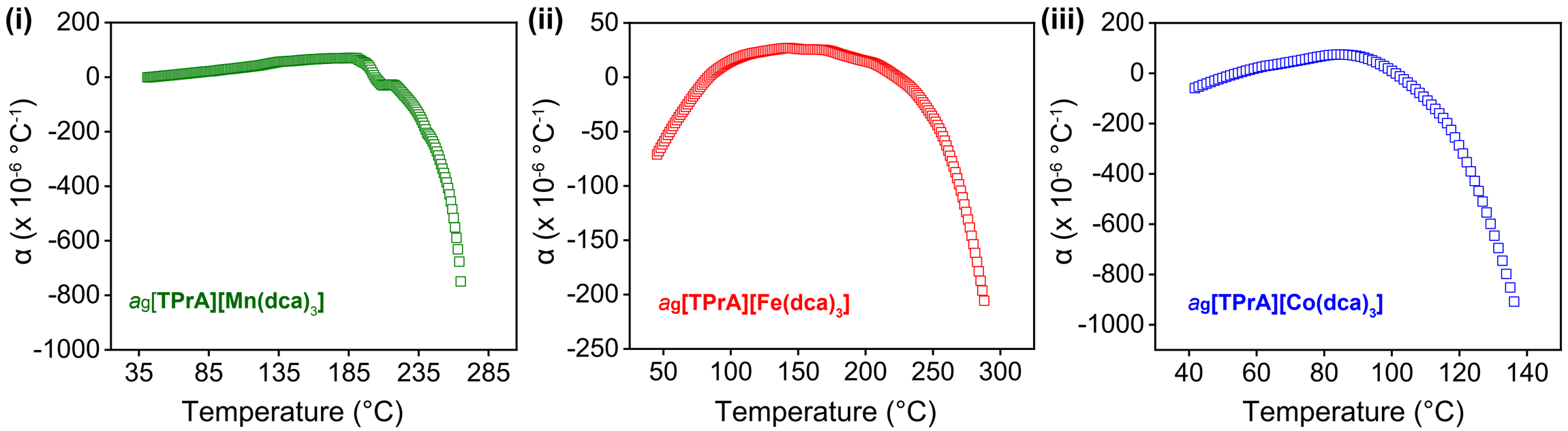
(i)
(ii)
(iii)
α (x 10-6 °C-1)
Temperature (°C)
ag[TPrA][Mn(dca)3]
ag[TPrA][Fe(dca)3]
ag[TPrA][Co(dca)3]

d

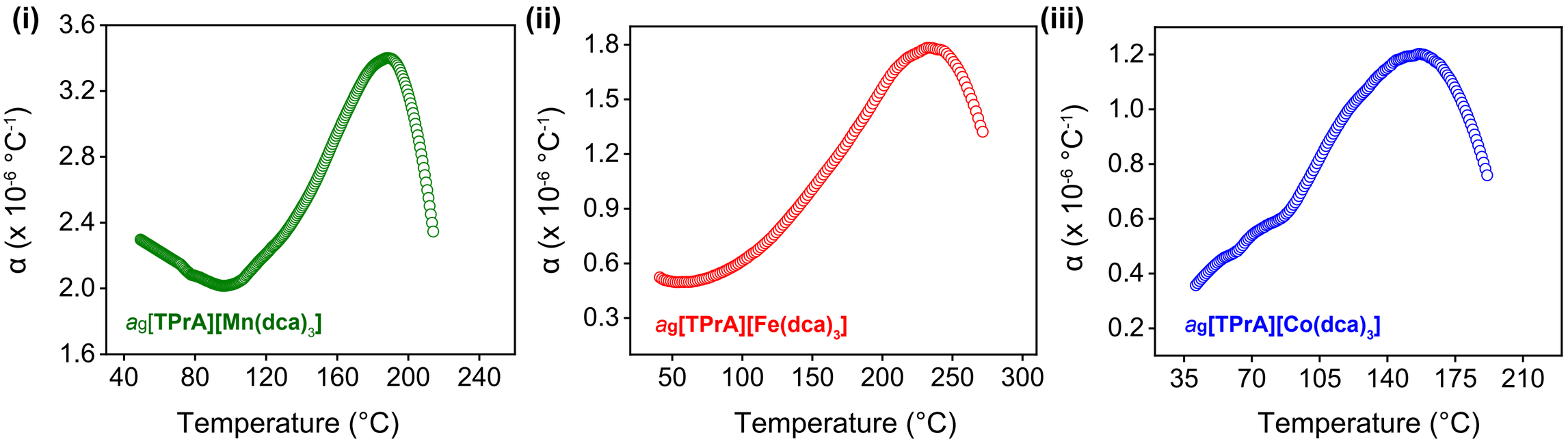
(i)
(ii)
(iii)
α (x 10-6 °C-1)
Temperature (°C)
ag[TPrA][Mn(dca)3]
ag[TPrA][Fe(dca)3]
ag[TPrA][Co(dca)3]

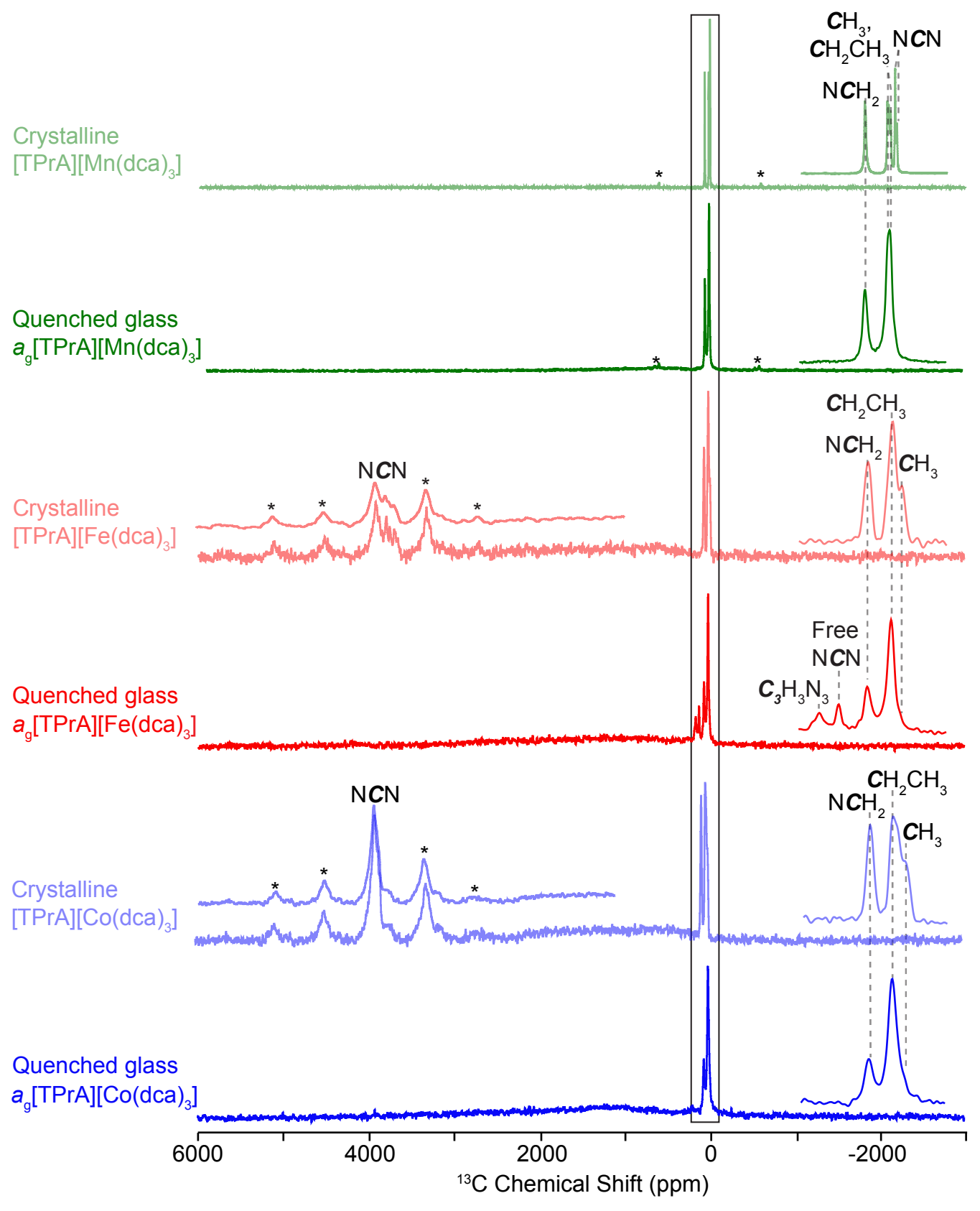
Crystalline
[TPrA][Mn(dca)3]
Quenched glass
ag[TPrA][Mn(dca)3]
Crystalline
[TPrA][Fe(dca)3]
Quenched glass
ag[TPrA][Fe(dca)3]
Crystalline
[TPrA][Co(dca)3]
Quenched glass
ag[TPrA][Co(dca)3]
CH3, CH2CH3
NCN
NCH2
CH2CH3
CH3
Free NCN
C3H3N3
6000
4000
2000
0
-2000
13C Chemical Shift (ppm)

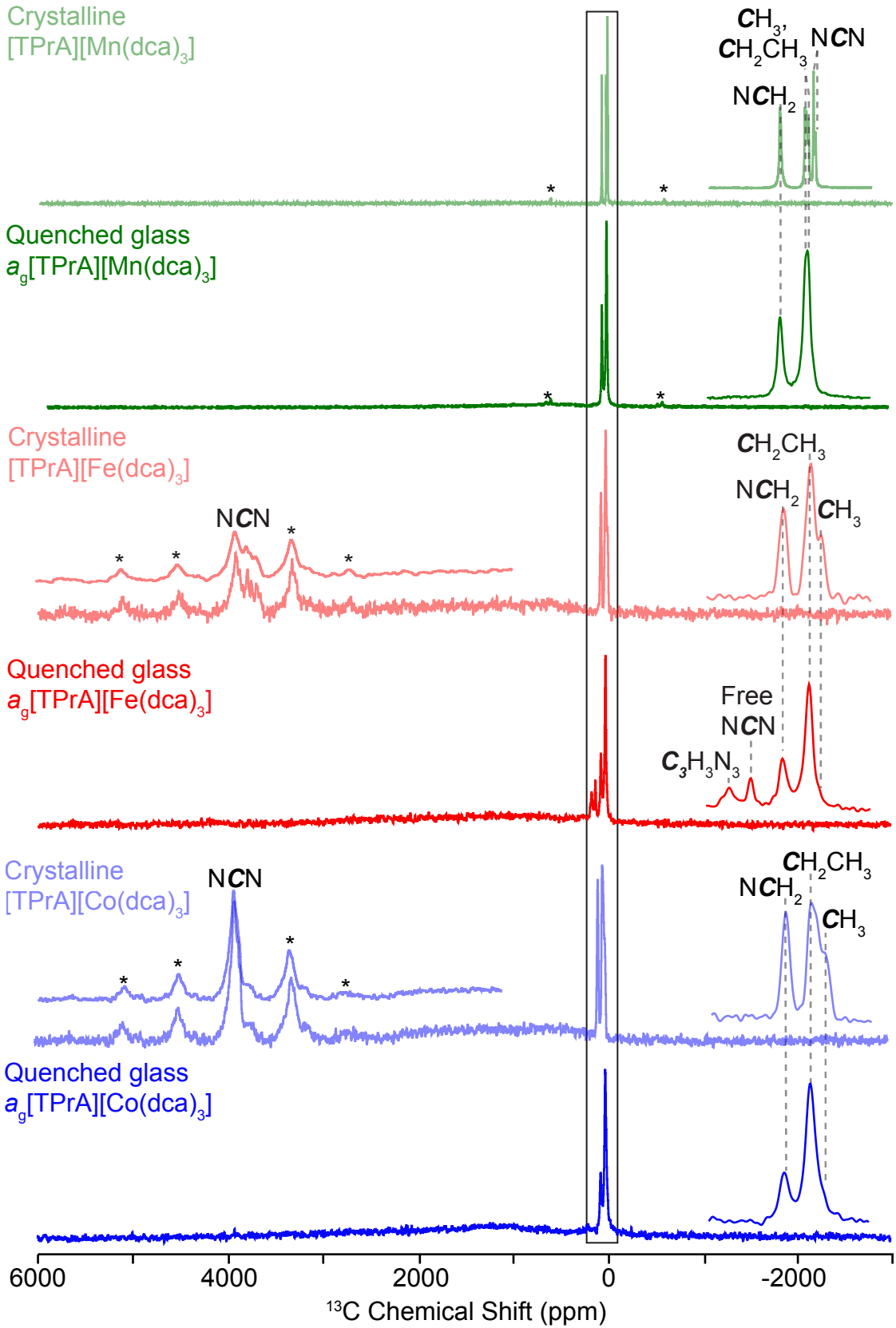
Crystalline
[TPrA][Mn(dca)3]
CH3,
CH2CH3
NCN
NCH2
*
*
Quenched glass
ag[TPrA][Mn(dca)3]
*
*
Crystalline
[TPrA][Fe(dca)3]
CH2CH3
NCH2
CH3
NCN
*
*
*
*
Quenched glass
ag[TPrA][Fe(dca)3]
Free
NCN
C3H3N3
Crystalline
[TPrA][Co(dca)3]
NCN
CH2CH3
NCH2
CH3
*
*
*
*
Quenched glass
ag[TPrA][Co(dca)3]
6000
4000
2000
0
-2000
13C Chemical Shift (ppm)

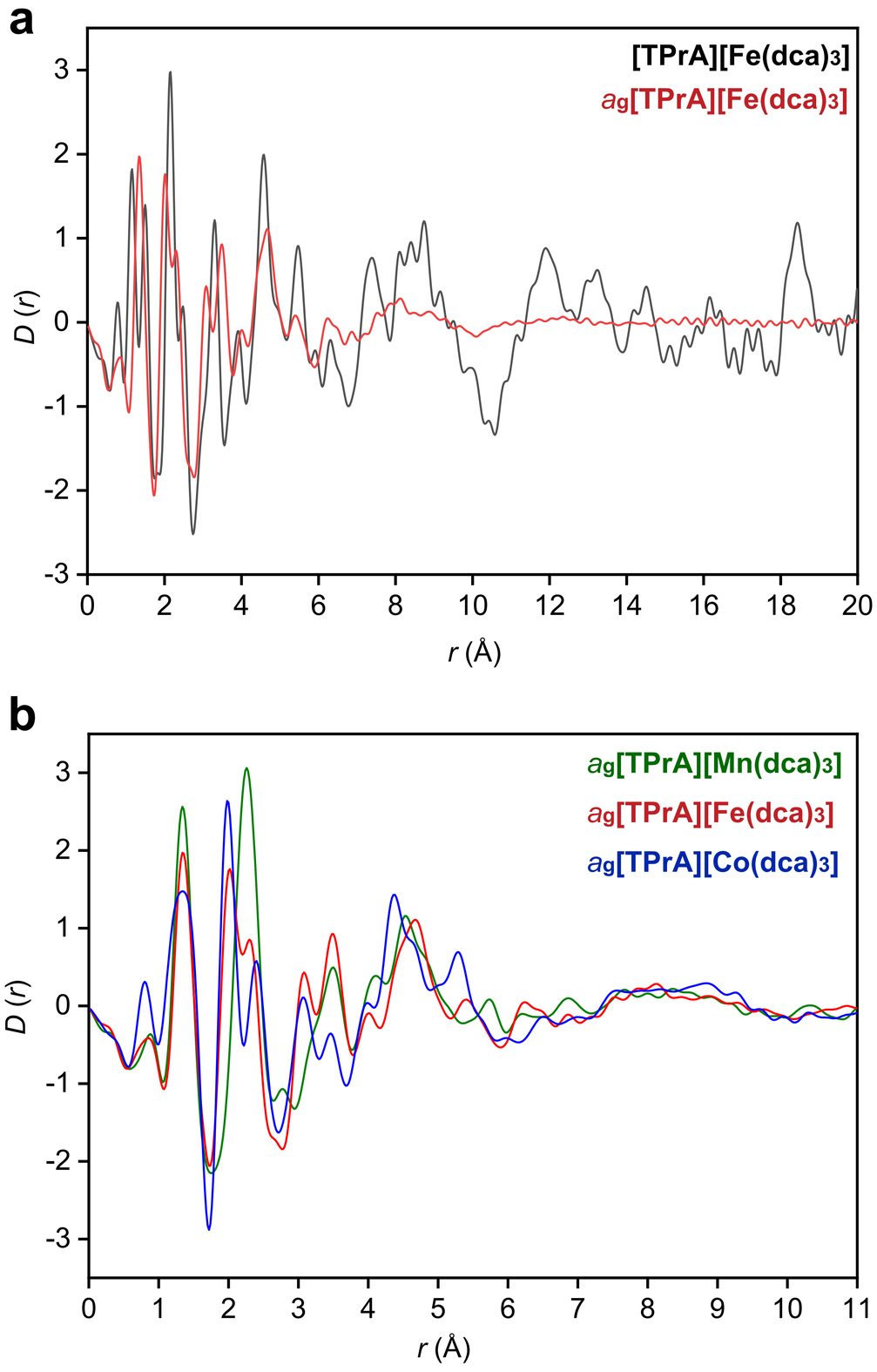
a
[TPrA][Fe(dca)3]
ag[TPrA][Fe(dca)3]
D (r)
r (Å)
b
ag[TPrA][Mn(dca)3]
ag[TPrA][Fe(dca)3]
ag[TPrA][Co(dca)3]
D (r)
r (Å)
c
300 K
750 K
1200 K
1700 K
gMn-N(r)
Mn–N distance (Å)
d
300 K
750 K
1200 K
1700 K
F(r) (kJ mol-1)
Mn–N distance (Å)
e
300 K
750 K
1200 K
1700 K
MSD(t) (Å2)
Time (ps)

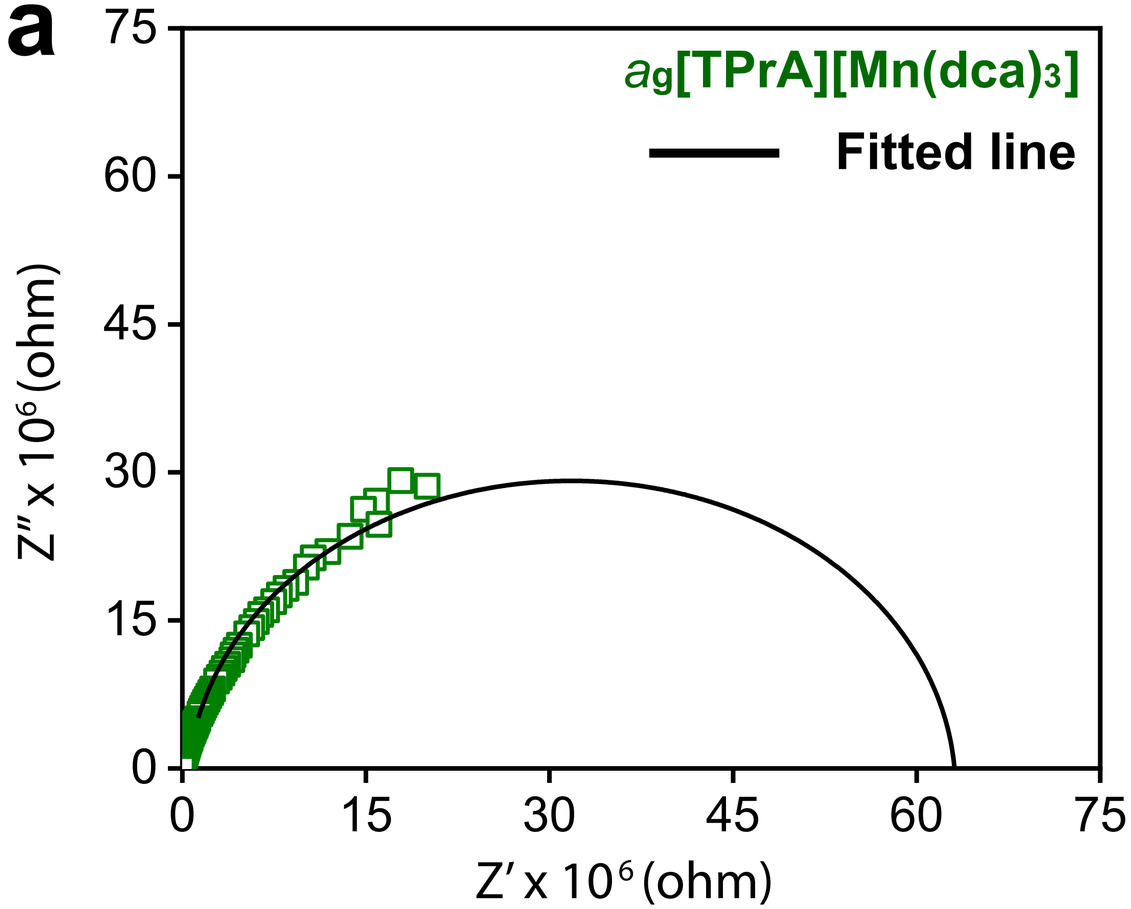
a
a_g[TPrA][Mn(dca)$_3$]
Fitted line
Z″ x 10^6 (ohm)
Z′ x 10^6 (ohm)
0
15
30
45
60
75

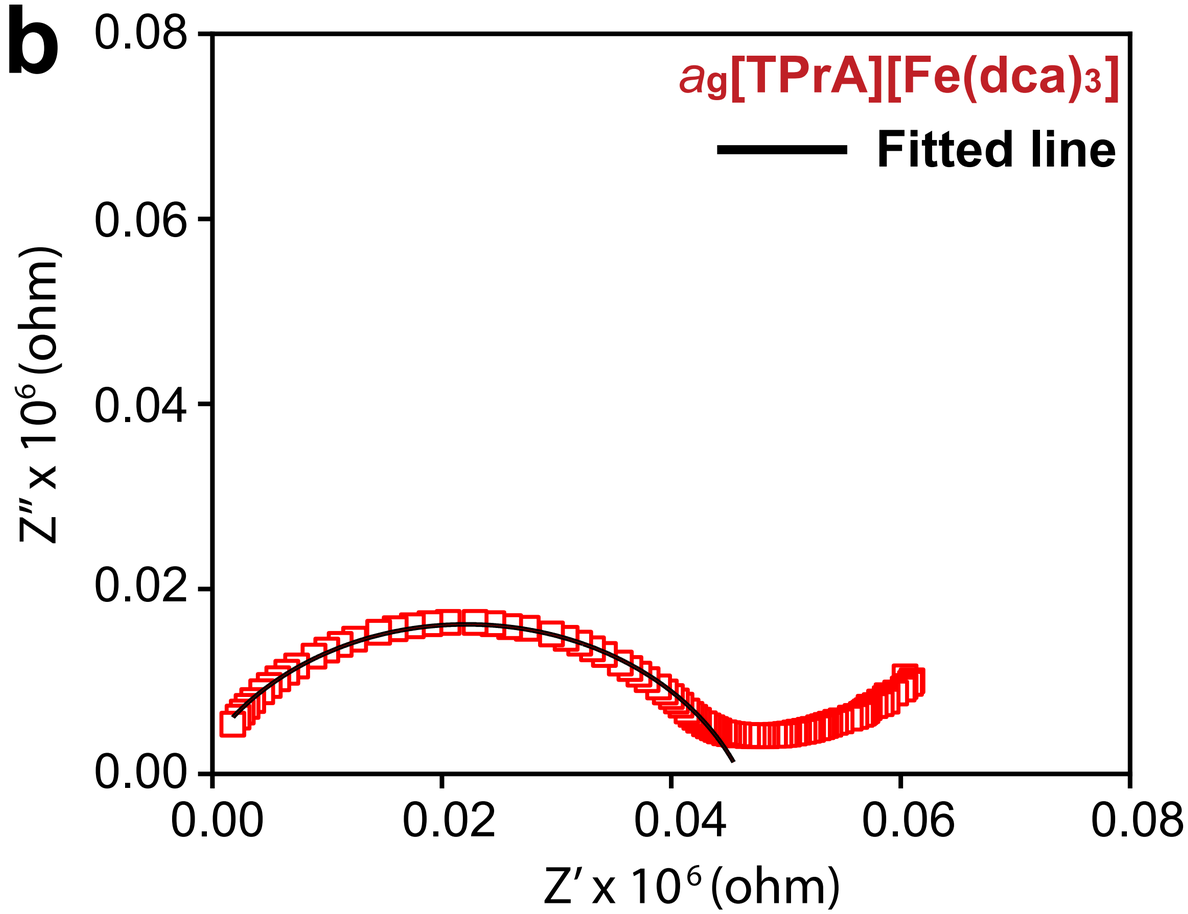
b
a_g[TPrA][Fe(dca)$_3$]
Fitted line
Z″ x 10^6 (ohm)
Z′ x 10^6 (ohm)
0.00
0.02
0.04
0.06
0.08

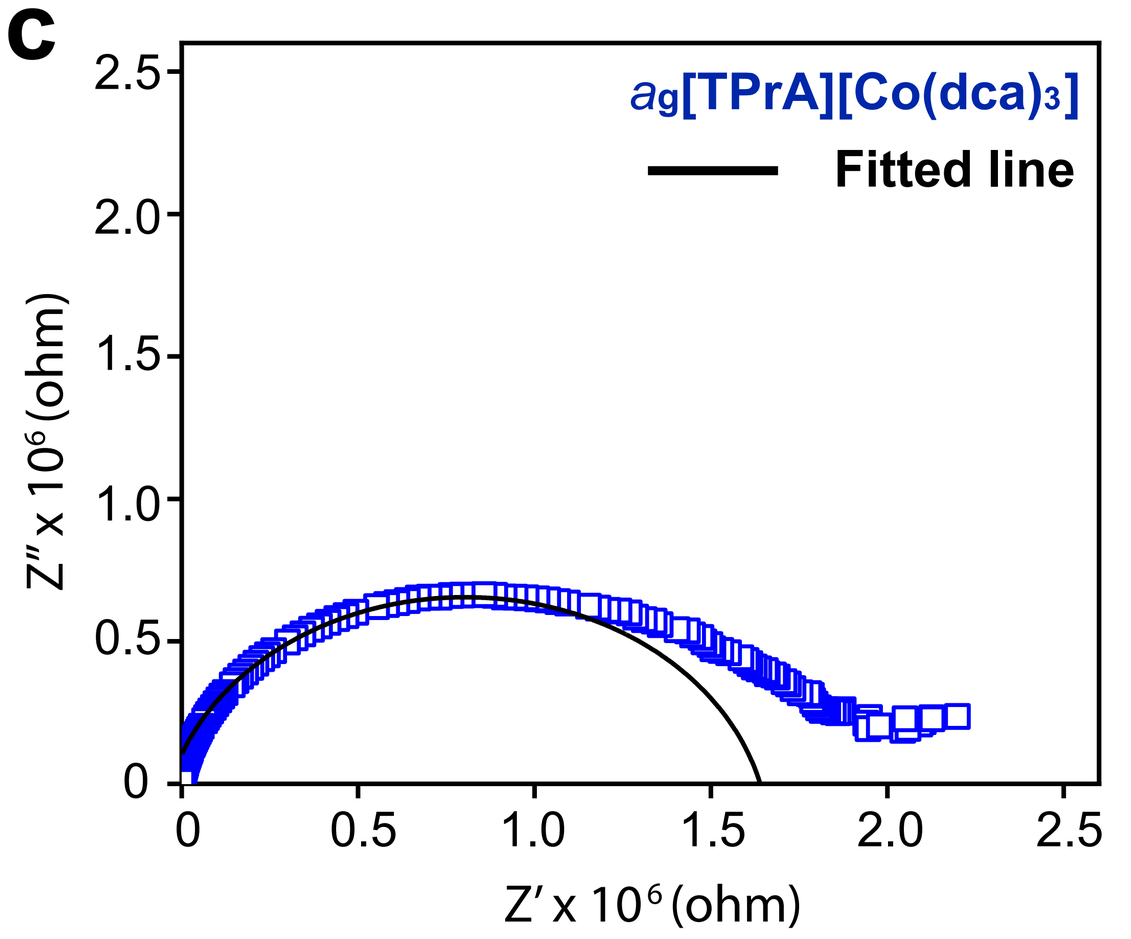
c
a_g[TPrA][Co(dca)$_3$]
Fitted line
Z″ x 10^6 (ohm)
Z′ x 10^6 (ohm)
0
0.5
1.0
1.5
2.0
2.5

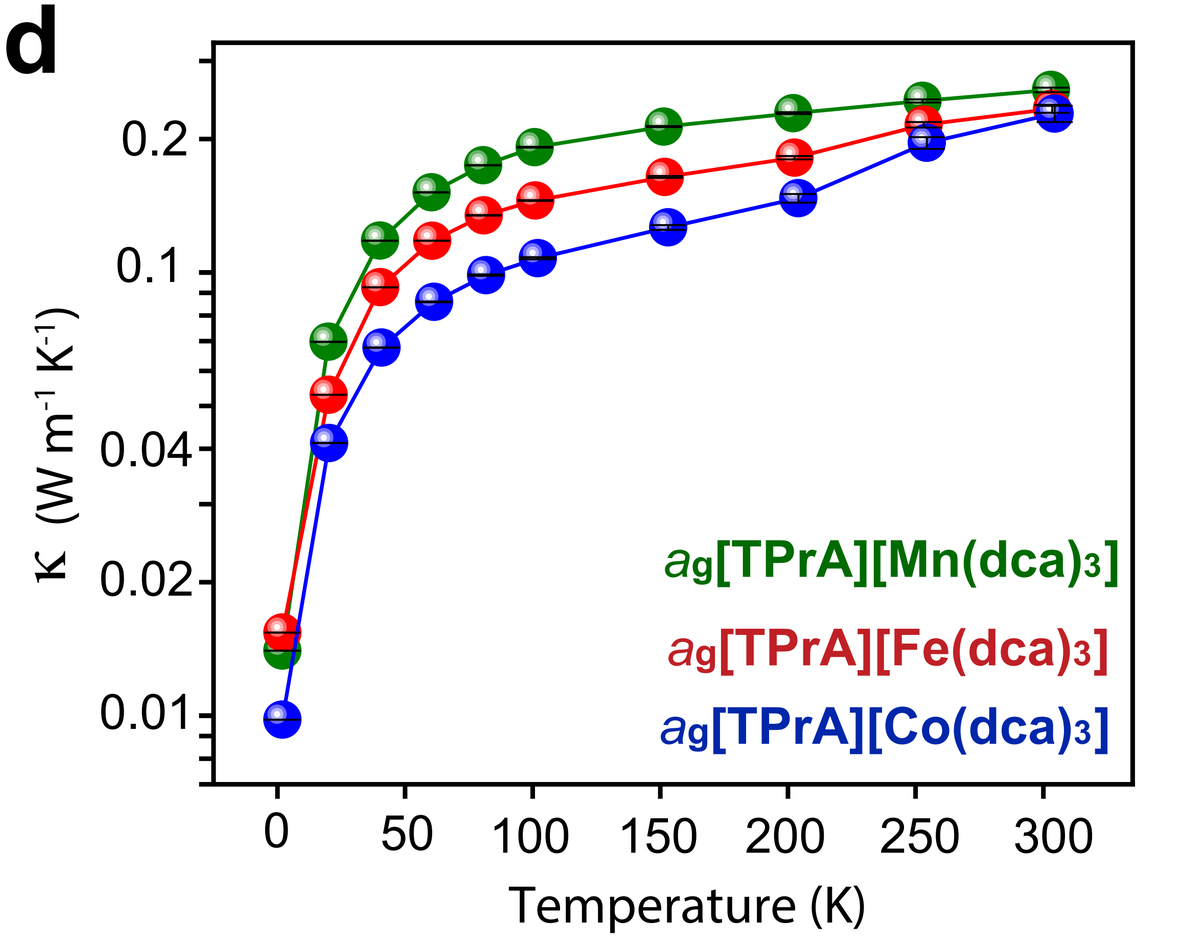
d
κ (W m^{-1} K^{-1})
Temperature (K)
a_g[TPrA][Mn(dca)$_3$]
a_g[TPrA][Fe(dca)$_3$]
a_g[TPrA][Co(dca)$_3$]
0.01
0.02
0.04
0.1
0.2
0
50
100
150
200
250
300

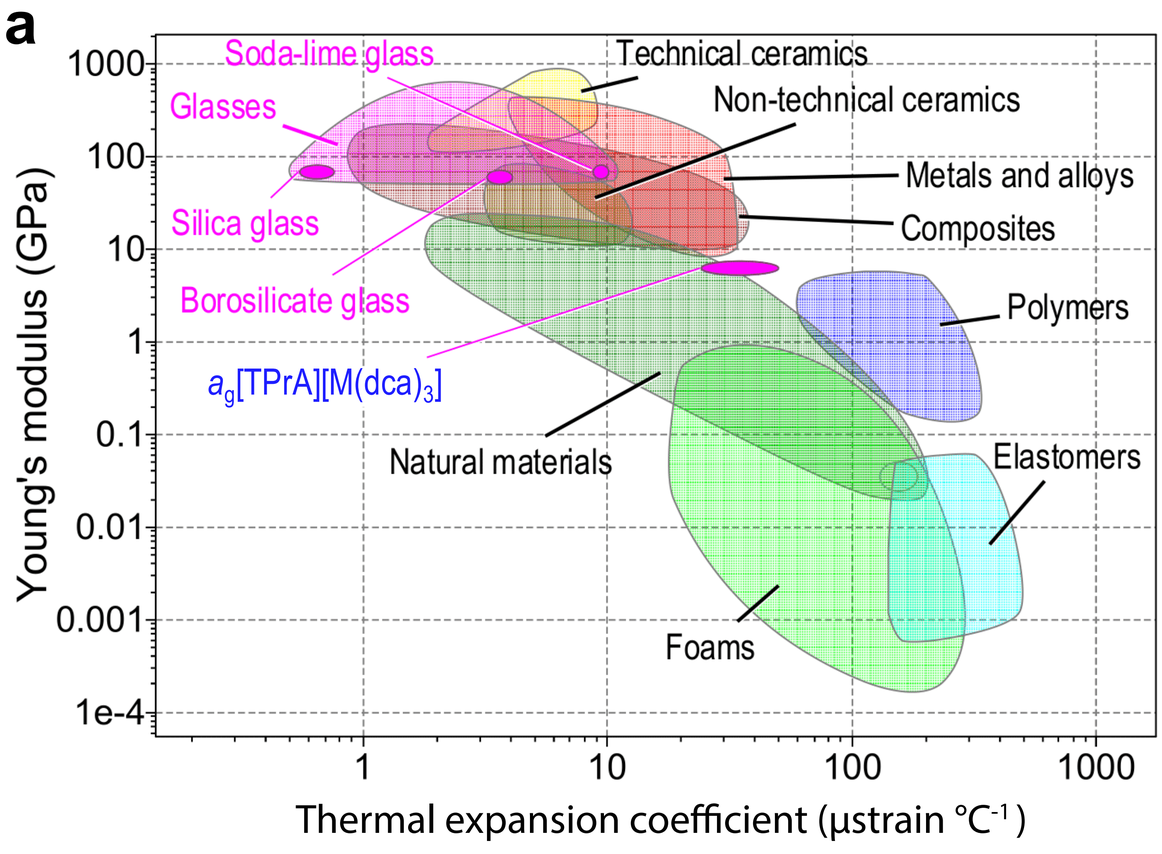
a
Soda-lime glass
Technical ceramics
Glasses
Non-technical ceramics
Metals and alloys
Silica glass
Composites
Borosilicate glass
Polymers
a_g[TPrA][M(dca)$_3$]
Natural materials
Elastomers
Foams
Young's modulus (GPa)
1000
100
10
1
0.1
0.01
0.001
1e-4
1
10
100
1000
Thermal expansion coefficient (μstrain °C^{-1})

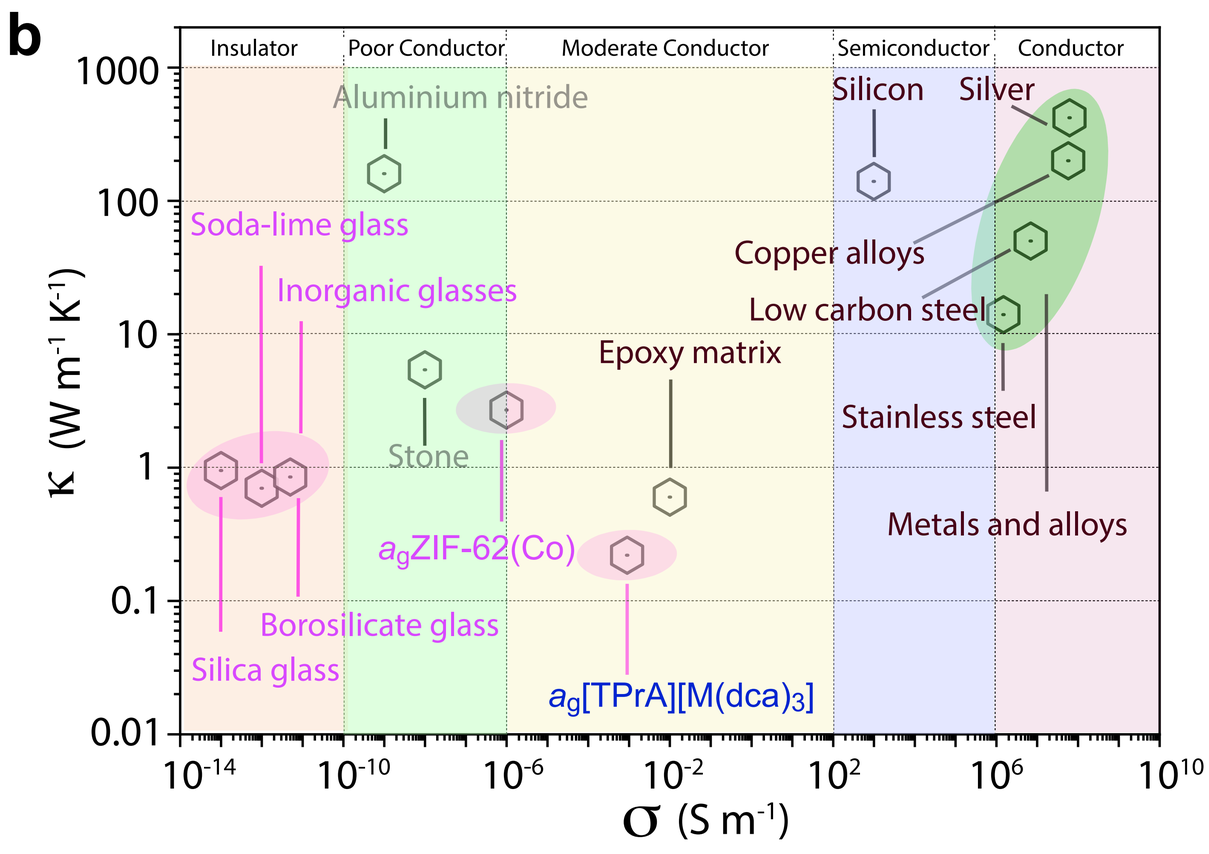
b
Insulator
Poor Conductor
Moderate Conductor
Semiconductor
Conductor
Aluminium nitride
Silicon
Silver
Soda-lime glass
Inorganic glasses
Copper alloys
Low carbon steel
Epoxy matrix
Stainless steel
Stone
Metals and alloys
a_gZIF-62(Co)
Borosilicate glass
Silica glass
a_g[TPrA][M(dca)$_3$]
κ (W m^{-1} K^{-1})
1000
100
10
1
0.1
0.01
10^{-14}
10^{-10}
10^{-6}
10^{-2}
10^{2}
10^{6}
10^{10}
σ (S m^{-1})